A multicellular actin star network underpins epithelial organization and connectivity

Barai Amlan, Soleilhac Matis, Xi Wang, Lin Shao-Zhen, Karnat Marc, Bazellières Elsa, Richelme Sylvie, Berrebi Dominique, Rümmele Frank, Théry Manuel, et al.

A multicellular actin star network underpins epithelial organization and connectivity

AUTHORS

Barai Amlan [1,2,3 &], Soleilhac Matis [1,2,3 &], Xi Wang [3], Lin Shao-Zhen [4 #], Karnat Marc [4 #], Bazellières Elsa [1], Richelme Sylvie [1], Berrebi Dominique [5,6], Rümmele Frank [7], Théry Manuel [8,9], Rupprecht Jean-François [4] and Delacour Delphine [1,2,3*]

[1] Aix Marseille Université, CNRS, UMR 7288, IBDM, Turing Center for Living Systems, Marseille, France

[2] Equipe labellisée Fondation ARC

[3] Université Paris Cité, CNRS, Institut Jacques Monod, F-75013 Paris, France

[4] Aix Marseille Université, CNRS, CPT (UMR 7332), Turing Centre for Living Systems, Marseille, France

[5] Paediatric Anatomo-Pathology Department, Hôpital Necker-Enfants Malades, Sorbonne Paris Cité, F-75015 Paris, France

[6] UFR de Médecine, Université Paris Cité, France

[7] Paediatric Gastroenterology Department, Hôpital Necker-Enfants Malades, Sorbonne Paris Cité, F-75015 Paris, France

[8] Université Paris Sciences et Lettres, CEA/CNRS, UMR8132, Ecole Supérieure de Physique et Chimie Industrielles de la Ville de Paris, Institut Pierre Gilles De Gennes, Paris France

[9] Université Grenoble-Alpes, CEA/INRA/CNRS, UMR5168, Interdisciplinary Research Institute of Grenoble, Grenoble, France

[&,#] Authors participated equivalently

* Corresponding author:
delphine.delacour@univ-amu.fr

KEYWORDS: epithelial morphogenesis, actomyosin, cell shape, supracellular cytoskeleton

SUMMARY

Epithelial tissues serve as physical barriers against various external pressures yet remarkably maintain structural stability. Various cellular apparatus including bicellular junction and actomyosin network contribute to the epithelial integrity, packing and remodelling. Although their role in morphogenetic and mechanical processes have been extensively studied during embryogenesis and disease development, their synergistic effects in maintaining tissue organization and connection remain poorly understood. In this study, we discovered a tissue-scale actomyosin network connected through bicellular junctions and manifested in the villi of adult murine intestinal tissue. Later we reproduced such supracellular structure in the differentiated compartment of *ex vivo* intestinal epithelium model. The self-organized actomyosin networks comprised individual actin nodes in each hexagonal cell at the epithelial base with six radial actin branches, presenting an 'actin star' unit. The repeated units were connected through the bicellular junctions, forming a large, multicellular array covering the differentiated domains. Functionally, actin stars contribute to epithelial morphological stability by maintaining cell hexagonality and packing, thereby preserving the solid-like order of the epithelium. Laser ablation experiments validate a modified vertex theoretical model that connects the emergence of such solid-like order to the onset of tension along the actin star branches. Actin stars also acted as locks at the basal side minimizing protrusive activity in the epithelial layer, hindering cell migration and disorganization of the epithelial tissue. The large actomyosin array also enhanced the long-range connectivity that ensure overall tissue integrity. Altogether, the supracellular actin star network constitutes a basal biomechanical apparatus coordinating epithelial tissue stability and organization.

INTRODUCTION

The actomyosin network ensures numerous morphogenetic processes through the generation and transmission of tension forces [1,2,3], which are primarily facilitated by the presence and activation of the molecular motor myosin-II (non-muscle myosin-II, NM-II) along actin filaments [4]. The pivotal functions of the contractile apparatus are particularly emphasized in epithelial tissues, which form resilient cellular assemblies lining the body surfaces. Monolayered epithelial behave as crucial interfaces between the internal milieu and the external environment, orchestrating essential physiological processes such as protection, secretion, and absorption. Thus, the preservation of epithelial tissue integrity stands as a paramount concern. Any disruptions in this integrity can yield profound consequences, including compromised organ formation and functionality, and potential tumorigenesis [5,6].

Epithelial monolayers possess distinct characteristics, marked by the polarization of densely packed cells into cohesive sheets. Hence, hexagonal packing represents an efficient way of covering a surface and distributing force equally among epithelial cells [7]. Moreover, cell polarization gives rise to discrete apical and basolateral domains, each endowed with unique molecular compositions and functions that dictate directional epithelial functions [8,6]. To maintain epithelial monolayer cohesion and coordination, cells establish robust intercellular junctions, notably adherens junctions mediated by cadherins and linked to actomyosin network via catenins, particularly enriched in the actin belt on apical side [9,10,11]. It is now clear that the apical coupling of E-cadherin, catenin and actomyosin is a powerful component for tissue mechanics, as it serves as a mechanosensor unit by responding to applied forces [11,12,13]. Therefore, the integration of mechanical information at the tissue level, achieved through adaptation of the actomyosin cytoskeleton or junctions themselves, is a major component of epithelial morphogenesis [11,13]. For instance, the apical-medial actomyosin drives apical constriction during mesoderm invagination in *Drosophila* embryos for apical area deformation. Apical constriction allows apical area deformation and ultimately tissue folding through mechanical forces applied on adherens junctions [14,15, 16,17,18]. In addition, anisotropic changes of tension along the cell surface control cell deformation that result in cell intercalation. During this process, cells remodel their junctions with neighbouring cells to permit cellular rearrangement during tissue elongation [19]. Altogether, these morphogenetic events directly impact the tissue physical state or tissue fluidity. Tissues in a solid-like state are barely remodelled and able to resist mechanical stress to maintain their architecture, while tissues in a fluid-like state are more prompt to remodelling due to exerted forces [20].

Here, we used the mammalian intestinal tissue to address mechanisms that control epithelial stability. We revealed the development of a multicellular star-shaped actomyosin lattice in the basal domain of differentiated epithelial cells, that behaves as a new mechanical unit at play for morphological and functional stability in the intestinal tissue.

RESULTS

Differentiated intestinal epithelial cells develop basal actin star-like structures

The mouse intestinal tissue is a suitable working model for investigating the collective organization of an adult mammalian epithelium. Its functional unit, known as the crypt-villus axis, exhibits distinct compartments: a proliferative domain represented by the crypt (in blue, Figure 1A) and a differentiated domain comprising the villus (in yellow, Figure 1A). Examination of adult mouse villi offered a direct glimpse into the *in vivo* organization of this columnar epithelium (Figure 1B). Through actin labelling in whole-mount tissue, we achieved a clear visualization of the brush border at the apical pole and the basolateral cell contacts (Figure 1B a,d). Notably, our observations revealed a regular actin meshwork located beneath the nuclei on the basal side of epithelial cells along the villus (Figure 1B b-d, Video S1). This meshwork comprised a dense actin core centrally located in each cell basal side, with discrete branches of actin bundles seemingly linking to cell-cell contacts (Figure 1B b-c). These ‘star-shaped’ actin-based structures were prevalent in the majority of epithelial cells along the villus, excluding those at the villus tip (not shown). Additionally, such 'actin stars' (AcSs) were conspicuously absent in crypt cells (Supplementary Figure 1A-C, Video S2), underscoring their specificity to the intestinal differentiated domain.

To delve deeper into the characterization of AcS structures and enhance their spatial resolution, we embarked on reproducing such network within a previously established 2D intestinal organoid culture [21]. In brief, organoid-derived monolayers were grown on soft substrates made of cross-linked (CL) Matrigel® matrix, on which they mimicked the patterning of intestinal tissue *in vitro* (Figure 1C). These include self-organizing crypt-like domains enriched with proliferative cells (i.e. EdU-positive cells, Supplementary Figure 1D), encircled by large villus-like domains with differentiated cells (i.e. cytokeratin-20- and ezrin-positive cells, Supplementary Figure 1E-F) [22,23,21]. Within the differentiated domain, we noticed a discernible brush border at the apical surface (Figure 1D a, Supplementary Figure 1F) and a similar star-shaped actin structure at the basal surface of each individual cell (Figure 1D b-c, Supplementary Figure 1F), mirroring our *in vivo* observations (Figure 1Bb-d). AcSs were notably absent in the crypt-like domain, like in the *in vivo* tissue (Figure 1D b,d, Supplementary Figure 1F). Thus, the development of basal AcSs network in the 2D differentiated domains

emulated those in the intestinal villi. The development of basal AcSs emerged as a significant hallmark of the differentiated domain in intestinal epithelium, alongside the apical brush border.

The assembly of basal actin stars creates an epithelial supracellular cytoskeletal network

Further structural analysis using high-resolution microscopy revealed that each epithelial cell of the differentiated domain exhibited a single AcS unit, featuring an actin node positioned at the centre of mass of the basal surface (Figure 2A,C) and accompanied by ~ 6 actin branches extending from it (Figure 2A-B,D). AcS branches measured approximately 5 µm in length (Figure 2E) and exhibited a regular radial organization, with a mean angle of α = 60±1.2° between actin branches (Figure 2F). Moreover, the actin branch was oriented perpendicular (β = 89±2°) to an adjacent bicellular contact (Figure 2A,B,F), and appeared to maintain directional continuity with a branch of the neighbouring cell's AcS (Figure 2B, insert). Consequently, the collective disposition of AcSs within the differentiated epithelial layer delineates a triangular network (Figure 2A-B) with AcS playing the role of a Delaunay tessellation of the Voronoi-like cell membrane network.

We could not detect canonical focal adhesion components, such as paxillin (Supplementary Figure 2A-B) or talin (not shown) at the AcS branches. While paxillin-positive focal adhesions were detected along actin fibres in cells located at the periphery of crypt-like domains, only faint and small paxillin dot patterns were observed in differentiated cells (Supplementary Figure 2A-B), suggesting that AcS branches are not primarily dedicated to cell-substrate adhesion. Subsequently, we examined the spatial arrangement of AcS branches at basal cell contacts. AcS branches from neighbouring cells did not exhibit physical continuity nor penetrate the plasma membrane (Figure 2B, insert). Instead, AcS branches snugly fit into finger-like medial membrane folds of bicellular membranes (Figure 2G-H, Supplementary Figure 2C), wherein E-cadherin-based adhesion sites and actin cross-linkers were localized (Figure 2Hc-e,I-J, Supplementary Figure 2C-E). This arrangement of finger-like and adhesive membranes at the extremities of AcS branches suggested a "zippering" effect at this level, potentially providing structural and architectural stability to the AcS network that connects each epithelial cell within the differentiated domain (Figure 2K).

Actin star formation relies on significant cell contractility and minimal substrate adhesion

Similar self-organizing structures resembling AcSs have been shown to emerge *in vitro* within minimal actin cortices on supported lipid layers, upon the addition of myosin-II filaments and

permissive contractility [24,25]. Consequently, we speculated that cell contractility might be a prerequisite in our system for the generation of AcSs. Analyses of myosin-IIA-KI-GFP organoid monolayers revealed a concentrated GFP signal at the AcS node and its surrounding area (Figure 3A-B). This finding was confirmed with endogenous phosphorylated myosin light chain 2 (P-MLC2) in 2D organoid monolayers (Figure 3C-D) and with endogenous myosin-IIA in adult mouse intestine (Supplementary Figure 3A). Notably, a substantial proportion of total cell contractility localised at the AcS level in the basal domain (Figure 3E), with approximately 61.5% of myosin-IIA-GFP and 61.3% of P-MLC2 signal intensity (Figure 3F). This suggests that the bulk of cell contractility accumulates at basal AcS structures. Furthermore, the contractile capacity of the differentiated cell type was particularly elevated compared to the proliferative cells of the crypt-like domain (Figure 3G), with myosin-IIA-GFP and P-MLC2 signal intensities averaging 1.30 and 2.37 times higher, respectively (Figure 3H). Similarly, P-MLC2 signal intensity was significantly lower in crypts compared to villi in adult small intestine (Supplementary Figure 3B-C). These data highlighted a distinct tissue patterning of contractility levels within this epithelium. Interestingly, live imaging analysis indicated that AcSs formed from actin foci that rapidly coalesced in cells that transverse the periphery of the crypt-like domain into the differentiated domain (Supplementary Figure 3D; Video S3). Thus, the emergence of AcS coincided with the transition of cells into a highly contractile tissue domain. Furthermore, we directly probed the necessity of contractility for AcS formation. Treating organoid-derived monolayers with blebbistatin, an inhibitor of actomyosin activity, resulted in the disappearance of typical AcS structures from the basal surface (Figure 3I). Under this condition, the actin cytoskeleton mainly organized along the lateral membranes and formed thin cables of stress fibers (Figure 3I). Similarly, inducible myosin-IIA-KO caused a significant dismantling of AcSs (Supplementary Figure 3E). In addition, restoring contractility in blebbistatin treated cells through subsequent wash-out led to the reformation of AcSs in approximately 30 min (Figure 3 J-K; Video S4). Live recording of actin cytoskeleton dynamics during this process revealed an active reorganization of actin cables (Video S5). Local inward contraction within each cell triggered the massive coalescence of actin into central foci and the accumulation of small actin bundles into thick radially arranged actin bundles, i.e. the forming AcS node and branches, respectively (Figure 3J; Video S5). Collectively, these findings pointed out the pivotal role of contractility in AcS generation and suggested that the star-like organization of the actomyosin network may be mechanically sensitive.

We then manipulated the mechanical environment of the organoid-derived monolayer by varying substrate rigidities using various polyacrylamide substrates (Matrigel-coated PAA gels) [26]. AcSs grew on soft substrates with a rigidity of 300 Pa (Figure 4A-B), a rigidity comparable to the *in vivo* condition [21]. However, stiffer substrates caused basal actin network remodelling, leading to the disappearance of AcSs (Figure 4A-B). Specifically, on 2.4 kPa

substrates, there was a shift towards the formation of numerous interconnected actin foci instead of a single actin node, while on 5.2 kPa substrates, stress fibre-like actin bundles predominated (Figure 4A-B). Thus, the mechanical properties of the cell substrate and subsequent cell-substrate adhesion level seem to be important for AcS formation.

To directly validate this hypothesis *in vitro*, we turned to a well-established intestinal epithelial cell line, adenocarcinoma Caco2 cells, in which the formation of AcS has not been previously documented. Initially, we grew Caco2 cells on stiff adhesion permissive substrates such as glass, and found canonical stress fibres instead of AcSs (Figure 4C, upper left panel). While Caco2 cells on soft CL-Matrigel substrates [21] (~300 Pa, comparable with the PAA gels used in Figure 4A) show significant loss of stress fibres (Figure 4C, upper right panel), AcS organization was still absent. We then elevated actomyosin contractility through calyculin-A treatment and discovered while no discernible modulation of the basal actin arrangement on the glass substrates (Figure 4C, lower left panel), the enhanced contractility caused the formation of AcS-like structures on soft CL-Matrigel substrates (Figure 4C, lower right panel). Of note, we found Caco2 cells developed large FAs (paxillin staining) on stiff substrates which were largely absent on soft crosslinked Matrigel substrates (Figure 4C). Along this line, we then tested if weakening cell-substrate adhesion might facilitate the development of AcS networks. We cultured these cells on micropatterned substrates featuring alternating adhesive and non-adhesive regions (Figure 4D). While Caco2 cells displayed conventional stress fibres on the adhesive areas, intriguingly, they developed patterns resembling AcSs on the non-adhesive regions (Figure 4E). These results suggest that lack of conventional cell-substrate adhesion facilitates the AcS network formation. Altogether, these results highlighted the critical roles of both mechanical properties of epithelial cells and their environment in AcS development, and suggested the existence of a critical force balance between the AcS lattice and cell-substrate adhesion. We concluded that the development of star-like actin structures likely arose from a combination of mechanical properties inherent to the intestinal epithelium: low adhesion to the substrate and high capacity for contractility.

The actin star network provides epithelial morphological and dynamical stability

What are AcS' functions in the epithelial tissue? We found that inhibition of AcS formation with blebbistatin treatment in the organoid derived monolayer induced a decrease in cell height (Figure 5A-B), indicating a shift from a columnar to a cuboid cell shape in the absence of the AcS network. Moreover, the treatment increased basal cell area (Figure 5C-D) and reduced cellular hexagonality, as quantified through a decrease in local triangular order (see Methods; Figure 5G). In addition, local inhibition of AcSs via light-inducible blebbistatin activation resulted in similar cell area modifications (Figure 5E-F). Conversely, the gradual re-

establishment of AcSs following blebbistatin treatment wash-out coincided with basal cell shape remodelling, characterized by the reduction of cell area and the acquisition of a more circular and hexagonal form (Supplementary Figure 4A-C; Video S6). Consistently, we observed an enhanced cell density within the epithelial tissue (Supplementary Figure 4D). Hence, AcSs likely contributed to the maintenance of a tightly packed columnar epithelial monolayer. Moreover, as shown in Figure 2B, 2G-J, AcSs contained in each epithelial cell were mechanically connected to each other via finger-like E-cadherin-based junctions on the basal surface, and we thus hypothesized that the AcS network may place the differentiated tissue under a homogenous tension.

To test this, we next incorporated our experimental observations into a computational model of the cellular assembly, called vertex model (see Supplementary Information). We first considered a coarse-grained model, where AcS formation triggers a homogeneous contractile response, through a reduction of the preferred cell area and cell perimeter (Figure 5G-H; Supplementary Information, Section I, Figure S1), in proportion set by experiments. As in experiments, we observed an increase in the level of hexagonality, as measured through the triangular order, within the cells undergoing the contractile stresses as compared to other cells (Figure 5I-K; Supplementary Information, Figure S6G; see Methods, section Computational modelling). This effect was reversible upon the removal of the contractile stress, thus mimicking the effect of blebbistatin. We also considered a second model where AcSs are modelled by a discrete set of force dipoles between the cell-cell junction midpoint and the cell barycentre (Supplementary Information, Section II, Figure S3). Such a second model leads to a similar path in the preferred area and perimeter space (see Supplementary Information, section II). These simulations also suggested that the resulting tissue was under high tension.

To experimentally assess the level of tissue tension, we next laser-dissected a single AcS and then monitored the behaviour of surrounding AcSs (labelled as actin nodes N1-6) (Figure 6A-B; Video S6). We found an almost immediate recoil of neighbouring AcS nodes after the ablation and existence of a visible recoil at large distances (Figure 6A-C). This indicated that, in the differentiated epithelial area, the AcSs of neighbouring cells were interconnected and allowed the transmission of tension beyond several rows of cells. Based on our vertex model simulation, in which a cell is ablated within a tensile tissue, we justified that the recoil speed is informative of the cell-substrate friction (Figure 6D-E). In our simulations, the delay in the strain propagation scaled with the distance to the ablated cell according to $\tau \sim L^2/K$, i.e. with K an effective diffusion of elasticity that is inversely proportional to the friction to the substrate (Figure 6F). These results showed a diffusion effect of the initial local elastic response after laser dissection and the existence of a mechanical diffusion of elasticity away from the ablation site, testifying of the large-scale connectivity provided by the AcS lattice.

Furthermore, we observed that the blebbistatin-treated organoid-derived monolayer displayed numerous and large basal cell protrusions resembling lamellipodia in the villus-like domain (pseudo-coloured in green, Figure 7A-B, t = 0 min). Upon recovery of contractility following blebbistatin wash-out, AcSs re-growth occurred (as discussed earlier), which was accompanied by the gradual disappearance of basal lamellipodia (Figure 7A-B t = 2 to 25 min; Video S5). We thus propose that AcSs might play a role in inhibiting basal cell dynamics. To directly test this hypothesis, we proceeded to laser dissection of a specific AcS and monitored its impact on the basal cell surface (Figure 7D). At 125s after AcS removal, the actin network reorganized and exhibited multiple actin foci within the cell which was targeted by laser dissection, indicating that AcS did not yet reformed. During this period, the basal cell surface expanded and exhibited actin-positive cell protrusions. Indeed, the perimeter of basal protrusive extension in the laser-dissected cell increased from 2.6±2.6 µm in the pre-ablation condition to 75.8±3.7. µm after the ablation (Figure 7C; Video S7). Based on these findings, we concluded that the AcS lattice restricted epithelial basal protrusive activity by placing the tissue under tension. These data prompted us to explore the participation of the AcS network to global epithelial tissue behaviour. As compared to the control condition, a blebbistatin treatment led to more persistent cell trajectories (Figure 7E), and more correlated velocities, both temporally (*D*, see Methods, Figure 7F-I), and spatially (*λ,* see *Methods,* Figure 7J). These observations were coherent within the generic theory of Henkes et al. [27], in which the increase of the protrusion persistence time *τ* drives an increase in the persistence of cell trajectories, as well as an increase in the velocity correlations *D* and *λ*. Collectively, these data demonstrated the functional impact of the AcS network which provides to the epithelial tissue a morphological stability, a mechanical connectivity and a long-range coordination.

DISCUSSION

Actomyosin star-shaped assemblies develop in differentiated intestinal epithelial cells

In this study, we unveil a supracellular star-shaped organization of actin network in mammalian intestinal epithelial cells and demonstrated its implication in various cellular and tissue functions (Figure 7K). To our knowledge, such actin meshwork development has not been previously documented in mammals, and contrast to the conventional basal actin organization, which predominantly exhibit stress fibres and/or lamellipodia [28,29,30]. However, some studies have reported unusual basal actin organization in specific contexts. In rat embryonic cells, geodesic-like arrangements of multiple actin foci transiently form before the formation of stress fibres, under the control of actin cross-linking factors (i.e. alpha-actinin, tropomyosin) [31].

Similar polygonal actin meshes, named cross-linked actin network (CLANs), organize in individual human trabecular meshwork cells [32,33]. In the same line, super-resolution imaging has shown a multitude of actin foci cortex organization within individual mouse embryonic stem cells [34]. Importantly, these structures did not denote a multicellular organization and were not regulated by myosin-II-mediated contractility; instead, they relied on actin polymerization. In addition, when mouse embryonic fibroblasts were cultured on non-adhesive/adhesive micropatterns, dynamic actin foci network developed on non-adhesive areas and were exacerbated under inhibition of actin polymerization [35]. Bershadsky and colleagues then showed through modelling that in this model system, myosin II-mediated contractility propels small actin assemblies towards each other, converging into a single large actin node [35]. Authors then hypothesized that multiple actin foci network may provide cytoskeletal connectivity to distal parts of the cell [35]. Furthermore, star-like actin networks have been previously reported *in silico* cell-free systems [24,36,37], where authors demonstrated that incorporation of myosin-II-based contractility on an F-actin monolayer induces the formation of a star-shaped actomyosin network and places the actin array under a 'dynamical steady state' [24,36,37]. Altogether, these studies underline how plastic the basal actin network can be in response to environmental factors [38]. They also pinpoint two pivotal factors: contractility and competition with cell-substrate adhesion, which may explain why AcS organization has not been observed yet in mammalians *ex vivo*. One possibility is that the conventional substrates employed in routine cell culture experiments are glass or plastic, which are exceedingly rigid and foster robust focal adhesions [39,40,41], impeding the formation of AcSs. In our experiments, we cultivated organoid-derived monolayers under conditions that closely emulate the *in vivo* rigidity, significantly softer than a typical cell culture dish [21]. However, using soft substrates alone was not enough to facilitate the formation of AcSs in the cancerous Caco2 cell line (Figure 4C). Another critical factor is the degree of contractility activation. Indeed, elevating contractility on a soft substrate provoked the appearance of AcSs in Caco2 cells. Similarly, intestinal differentiated compartments with heightened contractility, developed the AcS network, while low-contractile crypt compartments lacked AcSs (Figure 3G-H, Supplementary Figure 3B-C). Moreover, the AcS network was exclusively formed when organoid-derived monolayers were grown on soft substrates that hinder geodesic-like arrangements of multiple actin foci or mature focal adhesion formation (Figure 4A-B). Additionally, Caco2 monolayers displayed AcS formation under weakly adherent culture conditions solely when elevated contractility activation is induced via calyculin-A treatment (Figure 4E). It is tempting to suggest that these transformed/cancerous cells might have lost their innate capacity to promote optimal contractility, at least on the basal side when grown on soft substrate and in a weakly

adherent state. Subsequent experiments will be imperative for definitely clarifying this hypothesis.

The basal actin star assembly generates a supracellular connecting network

The AcS network may represent a distinctive multicellular mechanical entity within the basal region of differentiated epithelial cells. AcS self-organized structures were reminiscent of the apico-medial actomyosin, well-described in the Drosophila epithelium and which is required for cell shape remodeling through apical constriction [14,15,16,17,18]. Here, while the apical actin network remained localized to the subcortical zone behind adherent and tight junctions [11], the basal contractile AcS network extended in a more centripetal manner in intestinal epithelial cells at equilibrium, yet remained interconnected with E-cadherin-based junctions (Figure 2). When tension increases on the apical side, an apical-medial actomyosin network orchestrates tissue folding [14,15,16,17,18]. During intestinal development, apical constriction also occurs in mammalian intestine for crypt invagination [42,43,44]. It might be tempting to draw parallels with basal AcSs in differentiated intestinal epithelial cells, which naturally colonize curved geometry of villi in adults (Figure 1A), but AcSs also developed on flat surfaces in *in vitro* cultures (Figure 1D). This implies that they must serve functions beyond differentiated tissue folding.

In contrast to other epithelia, we and others showed that the majority of cell contractility is localized on the basal side of differentiated intestinal cells [44] (Figure 3E-F; Supplementary Figure 3B-C). Among the main differentiated gut cell types, the epithelial apical side gets specialized for nutrient absorption with the creation of a brush border of microvilli in enterocytes or for mucus secretion in goblet cells [45,46]. Although brush border anchors in the terminal web composed of actomyosin and intermediate filaments, this is a robust apical assembly that undergoes little remodelling in physiological conditions once formed, and for which a role for its contractile property outside of the context of brush border formation remains elusive [47,46, 48].

Star-shaped actomyosin assemblies on the basal cell surface have only rarely been described in epithelia. An ultrastructural study conducted by M. De Ceccatty in 1986 focusing on morphological investigations of sponge epithelial cytoskeletons, reported a similar star-shaped cytoskeletal organization on the basal epithelial layer [49]. Interestingly, our study echoes a recent study conducted by Harvey and colleagues [50]. These authors have also shown the presence of a basal-medial actomyosin network in Drosophila epithelium, which appears to be related to our AcS network. However, this study lacks a detailed characterization of basal actomyosin structures and their multicellular connectivity property, as the primary focus was on investigating a newly identified basal cell-cell adhesion complex named ‘basal spot junctions’ [50]. In the differentiated intestinal epithelium, AcS branches connected E-cadherin-based basal contacts that localized at structures between engulfed fingers and intercellular

bridges with basolateral cell-cell contacts, such as discussed by Svitkina and colleagues [51], testifying that AcS and basal contacts were under substantial tension. In addition, the presence of mechanosensitive elements like E-cadherin, β-catenin, α-catenin, vinculin, and α-actinin further hints towards the mechano-responsive nature of this network. The actin star network may thus represent a new way to create a more elastic communication system to transmit force imbalance through the tissue.

The actin star network constitutes a new mechanical apparatus for epithelial tissue organization and coordination

The AcS network represents a mechanical subunit at the basal cell side that connects surrounding epithelial cells. As such, it exerted functions at cellular and multicellular levels. At the cellular level, the AcS cytoskeletal lattice conferred morphological and functional stability to cells. It modulated cell shape by constraining the basal cell surface, thereby enhancing the columnar appearance and refining cell shape (Figure 5A-F; Supplementary Figure 4A-D). Additionally, it maximized epithelial cell packing and order (Figure 5G-K), which represents an important factor for stabilizing the epithelial assembly and optimizing the intestinal surface for nutrient absorption. Moreover, the disappearance of basal cell protrusive activity upon the formation of the AcS network suggested that AcSs restricted lamellipodia formation. Thus, the AcS network may facilitate cell transition from a motile, fluid-like, to a static, solid-like, morphology, as observed in mature epithelia [20]. To characterize this transition, we first considered the hexatic order which is a well-known measure in condensed matter [52]. Nevertheless, here we found that the triangular order, rather than the hexatic one, was the best probe of the AcS formation in experiments, and increased in active stresses in simulations (see Supplementary Information).

Beyond its cellular functions, the AcS network adopted a central role in orchestrating tissue architecture and homeostasis. By enhancing spatial coupling of differentiated epithelial cell clusters, it ensured the mechanical continuity of the epithelial monolayer, thereby upholding tissue integrity. Furthermore, the cytoskeletal network regulated cell shape, promoting a uniform cell hexagonalization that modulates established an epithelial order akin to a close-to-solid phase [20]. By constraining lamellipodia, AcSs hampered cell dynamics, pivotal for the formation of a tissue at equilibrium. This restriction mitigated random cell movement within the monolayer, leading to a relatively homeostatic and uniformly structured tissue architecture. In addition, at a broader tissue scale, the AcS network interconnected differentiated cells within the villus-like domain, and may facilitate the controlled collective cell movement observed along the crypt-villus axis [53]. An earlier study on gut epithelia turnover reported it to be mediated by actin-rich basal protrusions driven collective cell migration [54]. There, it was also

suggested that front-back polarity in the migrating cell is mediated by basal protrusions. Here, while observing the endogenous basal actin along the villi, we were unable to detect lamellipodial structures in the enterocytes. The majority of enterocytes were uniformly hexagonal and lacked front-back polarity. There was merely an evolution of the enterocyte basal cell shape at the very tip of the villus, which could resemble lamellipodial activity at that point (not shown) and might represent some active migrating cells.

In summary, we describe here a unique tissue-spanning multicellular organization of star-shaped actin networks in differentiated basal mammalian epithelium. Along the line of the De Ceccatty' hypothesis of "histoskeleton" in sponge [49], we believe that the AcSs represent a cytoskeletal network for coordination of mammalian epithelial tissue organization and its functioning. Our *in vivo* observations, as well as *ex vivo* and *in vitro* experiments, further confirmed the presence of this network in the intestinal epithelium, its mechanism of formation, and its essential role in tissue organization. We demonstrated that this network emerged under a high contractility / low cell-substrate adhesion state that naturally existed in the differentiated intestinal epithelium. We further showed its importance in regulating various functions from cell to tissue levels, that ensured tissue homeostasis and maintain healthy epithelial architecture. Together, this hints towards a mechanism of AcS network-mediated complex self-organization of the differentiated tissue.

Limitations of the study

While we showed the formation of actin stars in intestinal tissue, it is yet to be seen whether related structured networks also exist in other mammalian tissues. Notably, similar networks have been reported in sponge basal epithelium [49] and very recently in Drosophila epithelium [50]. Moreover, the only way to challenge AcSs at the moment is to modulate contractility. Although contractility is highly enriched at AcSs in differentiated intestinal cells, further characterization of these actomyosin structures will require the identification of core molecular components of AcS node and cables to specifically target them.

This study also raises the questions of how the dynamics of actin cables are coupled to the cell-cell junction rearrangement. While we show the network to be mechanoresponsive, further investigation would enlighten us about to what extent the network may regulate tissue mechanotransduction through basal junctions compared to apical mechanical apparatus. Furthermore, in-depth characterization of the contractile property of the AcS with optimal spatio-temporal resolution will be required to define whether these self-organized actomyosin assemblies are pulsatile or persistent, as described for the apico-medial actomyosin network in Drosophila [14].

Acknowledgments

We thank Ana-Maria Lennon-Dumenil, Robert S. Adelstein and Danijela Vignjevic for providing mice. We thank Arnaud Echard (Institut Pasteur, Paris), Guillaume Salbreux (UNIGE, Geneva), Benoit Ladoux, René-Marc Mège, Guillaume Romet-Lemonne and Antoine Jegou (IJM, Paris) for helpful discussions. Confocal microscopy and spinning-disc analyses were performed in the ImagoSeine microscopy facility (IJM) and PICSL imaging facility (IBDM). This work was supported by grants from the Groupama Foundation – Research Prize for Rare Diseases 2017 (to D.D), France 2030, the French Government program managed by the French National Research Agency (ANR-16-CONV-0001) and from the Excellence Initiative of Aix-Marseille University - A*MIDEX (to J.F.R.), as well as by ANR-20-CE30-0023 (COVFEFE) (to J.F.R.), the Fondation ARC (to M.S., J.S. and D.D), the Fondation pour la Recherche Médicale FRM (to A.B.), the Marie Skłodowska-Curie Actions, Postdoctoral Fellowships, project 101108750 (to A.B.), the Marie Skłodowska-Curie Actions Postdoctoral Fellowship, project 846449 (to W.X.), the Université de Paris IdEx UP 2021-I-050 funded by the French Government through its “Investments for the Future” (to D.D.), the ANR-19-CE13-0014-01 (to D.D.), the ANR-20-CE13-0015 (to D.D.), the Human Frontier Science Program (RGP0038/2018) (to D.D.), and the INCA PLBIO20-150 – Cancéropole Ile-de-France (to D.D.) and the CNRS through the MiTi interdisciplinary programs (to D.D.).

Supplemental Information: Supplementary Figures S1-S4, Videos S1-S7, and Supplementary Information file detailing the vertex model simulation procedure are in the online version of the paper.

Author contributions: A.B., M.S., W.X., S.Z.L., M.K., E.B., S.R., D.B., M.T., J.F.R. and D.D. designed and performed experiments and required analyses. A.B., M.S., S.Z.L., M.K., D.B., F.R., M.T., J.F.R. and D.D. coordinated the overall research and experiments, and wrote the manuscript.

Conflict of interest: The authors declare no conflict of interest.

FIGURE LEGENDS

Figure 1: Differentiated intestinal epithelial cells display star-shaped actin cytoskeleton. (A) Scheme showing the functional organization of the mouse small intestinal tissue where the proliferative crypt domains are shown in blue and the differentiated villus compartment in yellow. **(Ba-d)** Confocal analysis of actin distribution in the villus domain. Nuclei are stained in blue in (d). Green arrowheads point to actin stars (AcSs). Scale bars, (a) 50 µm, (b-d) 10 µm. **(C)** Scheme showing the self-organization of intestinal organoid-derived monolayer with the proliferative crypt-like domains in blue and the differentiated villus-like compartment in yellow. **(Da-d)** Confocal analysis of actin distribution in the apical or basal side of an organoid-derived monolayer. xz view is presented in (d). Crypt-like domains are delimited in blue. Green arrowheads point to actin stars. C, crypt-like domain. Scale bars, (a-b) 100 µm, (c) 10 µm, (d) 50 µm.

Figure 2: Basal actin star assembly creates a multicellular connecting network. (A) Airyscan confocal microscopy and depth-coded z-projection of actin, membranes and DNA localization in the basal side of organoid-derived monolayers. Scale bar, 10 µm. **(B)** N-SIM microscopy analysis of basal actin distribution in organoid-derived monolayers. Scale bar, 15 µm, insert 2 µm. **(C)** Statistical analysis of the distance between the AcS node and the cell center of mass in organoid-derived monolayers. Mean distance = 1.48±0.14 µm (mean±S.E.M). N = 3 experiments, n = 113 cells. **(D)** Statistical analysis of the number of actin branches per AcS. Mean number of actin branches per star = 6.04±0.07 (mean±S.E.M). N = 3 experiments, n = 90 cells. **(E)** Statistical analysis of the actin cable length in AcSs. Mean length = 5.16±0.06 (mean±S.E.M). N = 4 experiments, n = 331 cells. **(F)** Statistical analysis of the angle formed between actin cables (α) or between actin cables and plasma membranes (β). Mean α = 59±1.24° (mean±S.E.M), mean (β) = 89.3±1.78°. N = 4 experiments, n (α) = 162 cells, n (β) = 55. **(G)** Airyscan confocal analysis of actin (green), membranes (magenta) and DNA (blue) in organoid-derived monolayers. Scale bar upper row 5 µm, low row 2 µm. **(Ha-e)** Transmission electron microscopy analysis of the basal domain of differentiated cells in organoid-derived monolayers. Actin cables are pseudo-colored in green, adherens junction-like adhesions in light blue. ECM, extracellular matrix. Non-pseudo-colored images are shown in Supplementary Figure 2 C. Scale bars, (a) 5 µm, (b-c) 2 µm, (d-e) 0.5 µm. **(I-J)** Confocal analysis of E-cadherin and α-actinin-1 at the basal side of organoid-derived monolayers. Scale bar, 5 µm. **(K)** Scheme describing the architecture of AcS network (green) and cell membranes (magenta) in the basal side of organoid-derived monolayers. E-cadherin-based complexes observed in (H-I) are depicted in blue.

Figure 3: Cell contractility triggers actin star formation. (A) Confocal analysis of myosin-IIA-KI-GFP (magenta) localization in AcSs (green). Scale bar, 5 µm. **(B)** Statistical analyses of the signal intensity level of myosin-IIA-GFP in nodes and cables of AcSs. Normalized myosin-IIA-GFP signal intensity in AcS nodes = 0.666±0.01 (mean±S.E.M), in AcS cables = 0.034±0.001. N = 3 experiments, n = 154 cells. Mann-Whitney test, ****p<0.0001. **(C)** N-SIM analysis of P-MLC2 (magenta) localization in AcSs (green). Scale bar, 5 µm. **(D)** Statistical analyses of the signal intensity level of P-MLC2 in nodes and cables of AcSs. P-MLC2 signal intensity in AcS nodes = 0.743±0.038 (mean±S.E.M), in cables = 0.417±0.026. N = 3 experiments, n = 98 cells. Unpaired t-test, ****p<0.0001. **(E)** Confocal analysis of the apico-basal distribution of myosin-IIA-GFP (green) or P-MLC2 (magenta) in organoid-derived monolayers. Scale bar, 10 µm. **(F)** Statistical analyses of the signal intensity level of myosin-IIA-GFP and P-MLC2 in the apical and basal domain of differentiated cells. Mean apical myosin-IIA-GFP signal intensity in differentiated compartments = 725±48 (mean±S.E.M), basal myosin-IIA-GFP = 1159±72, apical P-MLC2 = 1314±63, basal P-MLC2 = 2078±135. N = 3 experiments, n (cells in differentiated compartments) = 23 cells. Two-way ANOVA, ****p<0.0001. **(G)** Confocal analysis of myosin-IIA-GFP (green) and P-MLC2 (magenta) distribution in an organoid-derived monolayer. Nuclei (DNA) are stained with Hoechst33342 (blue). Crypt-like domains (c) are delimited with a dotted blue line. Scale bar, 20 µm. **(H)** Statistical analyses of the relative signal intensity level of myosin-IIA-GFP and P-MLC2 in differentiated and crypt-like compartments. Mean myosin-IIA-GFP signal intensity in differentiated compartments = 2049±128 (mean±S.E.M), in crypt-like compartments = 1572±163, mean P-MLC2 signal intensity in differentiated compartments = 3644±224, in crypt-like compartments = 1536±176. N = 3 experiments, n (cells in differentiated compartments) = 23 cells, n (cells in crypt-like compartments) = 19 cells. Two-way ANOVA, *p = 0.012, ****p<0.0001. **(I)** Confocal analysis and z-projection of actin distribution in the basal domain of control or blebbistatin-treated organoid-derived monolayers. Scale bar, left panel 20 µm, right panel 10 µm. **(J)** Time-lapse images of CellMask actin (green) in tdTomato (magenta) organoid-derived monolayer after 1h blebbistatin treatment and then wash-out (t = 0min). Crypt-like domains (c) are delimited with a dotted blue line. Scale bar, 10 µm. **(K)** Statistical analysis of the mean time of AcS re-formation after blebbistatin treatment and wash-out. Mean time (min) = 51.41±1.67 (mean±S.E.M). n = 101 cells.

Figure 4: Epithelial mechanical properties and its environment condition on actin stars development. (A) Confocal analysis of the basal actin arrangement in organoid-derived monolayer grown on 300Pa, 2.4 or 5.2kPa PAA gels. Scale bar, 10 µm. **(B)** Statistical

559 analyses of basal actin-based structures formed on different rigidity PAA gels. Mean AcS
560 proportion at 300Pa = 33±10%, (mean±S.E.M), at 2.4kPa = 5.14±3.38%, at 5.2kPa = 0%.
561 Mean actin aster lattice proportion at 300Pa = 2±1.16%, at 2.4kPa = 14.14±3.95%, at 5.2kPa
562 = 12±3.34%. Mean actin stress fiber proportion at 300Pa = 0.67±0.67%, at 2.4kPa =
563 3.57±2.38%, at 5.2kPa = 16.62±6.36%. N = 3 experiments, n (300Pa) = 107 cells, n (2.4kPa)
564 = 160 cells, n (5.2kPa) = 229 cells. Two-way ANOVA, **p<0.01. **(C)** Confocal analysis of basal
565 actin (green), paxillin (red) and E-cadherin (magenta) in Caco2 cells grown on glass
566 coverslips, uncoated or on cross-linked Matrigel, and treated with either DMSO (control) or
567 20nM calyculin-A. Cells stained with phalloidin and paxillin show actin (green) or focal-
568 adhesion (red) organization respectively. Nuclei (blue) are stained with Hoechst33342. Scale
569 bar, 5 µm. Blue arrows show AcS nodes in Caco2 cells. Scale bar, 2 µm. **(D)** Scheme showing
570 the micropatterned substrates used for Caco2 monolayer culture in adhesive / non-adhesive
571 conditions. **(E)** Confocal analysis basal distribution of actin (green) and E-cadherin (magenta)
572 in Caco2 cells grown on adhesive / non-adhesive micro-patterns. Red dotted lines delimit the
573 adhesive from the non-adhesive areas. Blue arrows in the inset indicate AcS nodes. Nuclei
574 (blue) are stained with Hoechst33342. Scale bars, upper row 10 µm, lower row 5 µm.
575
576 **Figure 5: The actin star network ensures epithelial morphological stability. (A)** Confocal
577 analysis and xz view of actin distribution in DMSO-treated or blebbistatin-treated organoid-
578 derived monolayers. Nuclei (gray) are shown. Green arrowheads point to AcSs. Scale bar, 10
579 µm. **(B)** Statistical analysis of mean cell height in control or blebbistatin-treated cells. Mean
580 cell height in control = 10.79±0.33 μm^2 (mean±S.E.M), in blebbistatin-treated = 8.03±0.26. N
581 = 3 experiments, n (control) = 60 cells, n (blebbistatin-treated) = 65 cells. Unpaired t-test,
582 ****p<0.0001. **(C)** Statistical analysis of mean basal cell area in control or blebbistatin-treated
583 cells. Mean basal cell area in control = 69.56±1.25 μm^2 (mean±S.E.M), in blebbistatin-treated
584 = 83.69±1.96. N = 3 experiments, n (control) = 675 cells, n (blebbistatin-treated) = 585 cells.
585 Unpaired t test, ****p<0.0001. **(D)** Confocal analysis of actin distribution in DMSO-treated or
586 blebbistatin-treated organoid-derived monolayers. Nuclei (gray) are shown. Scale bar, 20 µm.
587 (**E)** Time-lapse of membranes-tdTomato before (green) and after (red) photo-activation of
588 azidoblebbistatin. Scale bar, 5 µm. **(F)** Statistical analysis of the basal cell area modification
589 after photo-activation of azidoblebbistatin. Mean basal cell area fold change in pre-activation
590 condition = 1.015±0.03 (mean±S.E.M), in post-activation condition = 2.353±0.21. N = 3
591 experiments, n (pre-activation) = 23 cells, n (post-activation) = 10 cells. Unpaired t-test,
592 ****p<0.0001. **(G)** Mechanical description of the AcS network contractility within a cell by active
593 stresses. Here, $T_i = \zeta s_i$ (with $\zeta>0$) is the active tension mimicking the active contractility of actin
594 bundles. This can be further simplified to be active tensions T along the cell contour and active

595 cellular bulk stresses σ_a. **(H)** Theoretical analysis of cell anisotropy dictated by the active
596 pulling stress α and the active tension χ. The black solid line represents the theoretically
597 predicted critical rigidity transition line; see Eq. (S19) in Supplementary Information. The
598 symbols and arrow denote a possible path of cell differentiation. **(I)** Variation of the local
599 triangular order parameter map upon AcS formation and subsequent optimal cell
600 differentiation, or AcS inhibition under blebbistatin treatment and deficient cell differentiation.
601 **(J)** Statistical quantification of the local triangular and hexatic order *in silico.* **(K)** Statistical
602 quantification of the local triangular and hexatic order from experiments.
603
604 **Figure 6: The actin star network provides mechanical connectivity and long-range**
605 **coordination. (A)** Color-coded time-lapse analysis of AcS displacement after laser ablation
606 of a given AcS (white circle). The first image (t = -10s) is false-colored green, the image at a
607 given time, i.e. before (t = 0s) or after (t = 1, 25 or 60s) laser ablation is false-colored in red.
608 Masks of AcS nodes are also presented in the lower panel. Scale bar, 10 µm. **(B)** Scheme
609 showing the site of laser ablation with dotted circle in the AcS lattice (green) within the
610 epithelial monolayer (magenta), and depicting the AcS nodes (N) annotation for quantification.
611 **(C)** Average radial displacement of AcS nodes that neighbour the laser ablation point. N0,
612 point of AcS laser-ablation. **(D)** Upper panel, sketch of the active vertex model with cell-cell
613 junction viscosity. Lower panel, laser ablation protocol: the cell at the model ablation site has
614 its activity set to zero. **(E)** Average radial displacement of cell barycentres at the *N*-th row as
615 a function of time *t* after ablation (see Methods). **(F)** Time to reach 0.20 µm radial
616 displacement, $t_{0.2\mu m}$, (mean ± S.E.M) as a function of the row of cells (i.e., distance to the laser
617 ablation site), in experiments (blue, *n* = 13 – 18 tracked AcS nodes) and simulations (red,
618 averaged over *n* = 5 independent simulations).
619
620 **Figure 7: The actin star assembly restricts epithelial dynamics. (A)** Time-lapse of
621 CellMaskActin (white) and membranes-tdTomato (red) organoid-derived monolayer after 1h
622 blebbistatin treatment and then wash-out (t = 0 min). Actin-based protrusive structures are
623 outlined in green, and also shown in the lower black and white panel. Yellow arrowheads point
624 to actin-based protrusive extension. Scale bars, 10 µm. **(B)** Statistical analysis of cell perimeter
625 protrusive before and after blebbistatin wash-out. Mean perimeter protrusive before =
626 42.37±1.92 (mean±S.E.M), after = 3.64±0.78. N = 4 experiments, n = 100 cells. Paired t-test,
627 ****p<0.0001. **(C)** Statistical analysis of the perimeter of basal protrusive cell extension after
628 laser ablation of the AcS node. Mean perimeter in pre-ablation condition = 2.612±2.61
629 (mean±S.E.M), in post-ablation condition = 75.83±3.69. N = 3 experiments, n = 8 cells.
630 Unpaired t-test, ****p<0.0001. **(D)** Time-lapse of CellMaskActin (green) and membranes-

tdTomato (red) before or after laser ablation (blue dotted circle) of an AcS node. Cell perimeter is outlined before ablation in yellow dotted line and after ablation in red dotted line. Yellow arrowheads point to actin-based protrusive extension. Nuclei are stained in blue. Scale bar, 5µm. **(E)** Automated cell tracking in DMSO- or blebbistatin-treated tdTomato organoid-derived monolayers, and t-projection of 20 frames time-lapse series. Monolayer background corresponds to t = 0. Scale bar, 20 µm. **(F)** Statistical analysis of the mean cell strain in DMSO-treated or blebbistatin-treated organoid-derived monolayers. Mean cell strain in DMSO-treated cells = 0.159±0.0003 (mean±S.E.M), in blebbistatin-treated = 0.187±0.0007. n (DMSO-treated cells) = 95863, n (blebbistatin-treated cells) = 21950. Mann-Whitney test, ****p<0.0001. **(G)** Statistical analysis of the mean cell velocity in DMSO-treated or blebbistatin-treated organoid-derived monolayers. Mean velocity in DMSO-treated cells = 0.123±0.002 µm/min (mean±S.E.M), in blebbistatin-treated = 0.183±0.004. n (DMSO-treated cells) = 3116, n (blebbistatin-treated cells) = 1622. Mann-Whitney test, ****p<0.0001. **(H)** Statistical analysis of the mean diffusion coefficient in DMSO-treated or blebbistatin-treated organoid-derived monolayers. Mean diffusion coefficient in DMSO-treated cells = 0.015±0.003 (mean±S.E.M), in blebbistatin-treated = 0.044±0.009. n (DMSO-treated cells) = 4, n (blebbistatin-treated cells) = 3. Unpaired t-test, *p=0.0159. **(I-J)** Analysis of velocity correlations in DMSO-treated or blebbistatin-treated organoid-derived monolayers: **(I)** autocorrelations, as a function of time, **(J)** same-time correlations, as a function of the point-to-point distance (see Methods). N = 4 in DMSO-treated and N = 3 in blebbistatin-treated experiments. **(K)** Scheme depicting the proposed model of AcS development in the mammalian intestinal epithelium.

SUPPLEMENTARY FIGURE LEGENDS

Supplementary Figure 1: (A-C) Confocal analysis of actin distribution in the mouse crypt compartment. Crypt side view (B) and bottom view (C) are shown. Crypt domains are delimited with blue line. L, crypt lumen. Scale bar A 100 µm, B-C 10 µm. **(D-E)** Confocal analysis of EdU (D) and cytokeratin-20 (E) distribution in organoid-derived monolayers. Nuclei are sown in gray. Crypt-like domains are delimited in blue. C, crypt-like domain. Scale bar (D), 20 µm, (E) 30µm. Scale bar, 100 µm. **(F)** Confocal analysis of actin (green), ezrin (magenta) and DNA (gray) in the apical or basal side of organoid-derived monolayers. Crypt-like domains are delimited in blue. C, crypt-like domain. Scale bar, 20 µm.

Supplementary Figure 2: (A-B) Airy scan confocal analysis of paxillin (magenta) and actin (green) in the area of crypt- / villus-like boundary or in the differentiated compartment. Crypt-like domains are delimited in blue. C, crypt-like domain. Scale bar, 10 µm. **(Ca-e)** Transmission electron microscopy analysis of the basal domain of differentiated cells in organoid-derived monolayers. ECM, extracellular matrix. Scale bars, (a) 5 µm, (b-c) 2 µm, (d-e) 0.5µm. **(D-E)** Confocal analysis of β-catenin (magenta) or α-catenin (magenta) and actin (green) in the differentiated compartment of organoid-derived monolayers. Scale bar, 5µm.

Supplementary Figure 3: (A) Confocal analysis of actin (green) and myosin-IIA (magenta) in the basal domain of differentiated cells along the villus of the mouse small intestine. Scale bar, 5 µm. **(B)** Confocal analysis of P-MLC2 distribution in the human intestinal tissue. Areas boxed in yellow are presented on the right. Scale bar, 200 µm. **(C)** Statistical analyses of the signal intensity of P-MLC2 in the villus epithelium and the crypt epithelium in the human small intestine. Mean normalized signal intensity in the villus epithelium = 1, in the crypt epithelium = 0.5691±0.021. N (intestinal biopsies) = 3. Unpaired t-test, ****p<0.0001. **(D)** Time-lapse analysis of AcS formation at exit of the crypt-like domain in organoid-derived monolayers. Actin (green) and membranes (red) are shown. Yellow arrowheads point toward one AcS formation. Crypt-like domains are delimited in blue. C, crypt. Scale bar, 10 µm. **(E)** Confocal analysis of actin distribution in mosaic myosin-IIA-KO organoid-derived monolayers. Myosin-IIA-KO-induced cells are positive for membranes-mG (green). Crypt-like domains are delimited in blue. C, crypt. Areas boxed in yellow are presented on the right. Scale bar, 20 µm.

Supplementary Figure 4: (A) Time-lapse of CellMaskActin and membranes-tdTomato organoid-derived monolayer after 1h blebbistatin treatment and then wash-out (t = 0min). Color-coded t-projection of time-lapse series of membranes-tdTomato signal at the basal domain during contractility recovery in organoid-derived monolayer is shown (t=0min in green,

t = 46 min in red). Scale bar, 10 µm. **(B)** Statistical analysis of basal cell area before and after blebbistatin wash-out. Mean basal area before = 141.75±5.67 (mean±S.E.M), after = 95.67±3.69. N = 4 experiments, n = 100 cells. Paired t-test, ****p<0.0001. **(C)** Statistical analysis of basal cell circularity before and after blebbistatin wash-out. Mean basal circularity before = 0.70±0.01 (mean±S.E.M), after = 0.79±0.01. n = 100 cells. Paired t-test, ****p<0.0001. **(D)** Statistical analysis of cell density before and after blebbistatin wash-out. Mean cell density before = 7.65±0.79 (mean±S.E.M), after = 9.40±0.93. Paired t-test, **p=0.004.

SUPPLEMENTARY VIDEOS

Video S1: Z-stack confocal imaging of actin distribution through the differentiated epithelial monolayer of the villus compartment in the adult mouse small intestine. Left panel, distance between z-slices, 0.42 µm. Scale Bar, 20 µm. Right panel, distance between z-slices, 0.23 µm. Scale bar, 5 µm.

Video S2: Z-stack confocal imaging of actin distribution through the proliferative epithelial monolayer of the crypt compartment in the adult mouse small intestine. Distance between z-slices, 0.23 µm. Scale bar, 10 µm.

Video S3: Time-lapse imaging of CellMask-Actin-GFP (green) and Membranes-tdTomato (magenta) during cell exit from the crypt-like domain and cell entry in the differentiated domain of organoid derived-monolayers. White arrowheads point toward one AcS formation. Crypt-like domains are delimited in yellow circle. Right side shows magnified region of interest. Scale bars, 10 µm (left) and 5 µm (right). Images were acquired every 3 min. Frame rate is 4 fps.

Video S4: Time-lapse imaging of CellMask-Actin-GFP (green) and Membranes-tdTomato (magenta) in organoid derived-monolayers after blebbistatin treatment and subsequent wash-out. Scale bar, 20 µm. Images were acquired every 120 s. Frame rate is 10 fps.

Video S5: Time-lapse imaging of CellMask-Actin-GFP (inverted grey or green) and Membranes-tdTomato (magenta) in organoid derived-monolayers after blebbistatin treatment and subsequent wash-out. Scale Bar, 10 µm. Images were acquired every 120 s. Frame rate is 10 fps.

Video S6: Time-lapse imaging of CellMask-Actin-GFP (grey) in organoid derived-monolayers after laser ablation of around a single AcS node along the yellow circle. Tracked AcS nodes trajectories from ablation center are indicated with colored lines, with node '1' (N1) in red indicating immediate neighbour to the ablated node, N2 in green neighbouring N1, N3 in cyan neighbouring N2, N4 in blue neighbouring N3, N5 in magenta neighbouring N4, N6 in yellow neighbouring N5. Scale bar, 10 µm. Images were acquired every 1.1 s. Frame rate is 10 fps.

Video S7: Time-lapse imaging of CellMask-Actin-GFP (inverted grey or green) and Membranes-tdTomato (red) and Hoechst 33342 stained nucleus (blue) in organoid derived-monolayers after laser ablation around a single AcS node indicated with orange circle. Scale bar 10 µm. Images were acquired every 1.56 s. Frame rate is 10 fps.

STAR METHOD

RESOURCE AVAILABILITY

Lead contact

Further information and requests for resources and reagents should be directed and will be fulfilled by the lead contact Delphine Delacour (delphine.delacour@univ-amu.fr).

Materials availability

Materials generated in the current study are available from the lead contacts upon request. There are restrictions to the availability of due to collaborations or MTAs.

Data and code availability

Source data files have been deposited at XXX and are publicly available as of the date of publication. The DOI is listed in the key resources table. Microscopy data reported in this paper will be shared by the lead contact on request. Any additional information required to re-analyze the data reported in this paper is available from the lead contact upon request.

EXPERIMENTAL MODEL AND SUBJECT DETAILS

Organoid cultures and transfection

Wild-type C57/Bl6 adult male mice were provided by the animal house facility of the Institut Jacques Monod and by Charles River company (France). Mice were housed in EOPS (Environment without Specific Pathogenic Organisms) environment, and handled in accordance with French regulation for animal care. VillinCreERT2-tdTomato organoids were generated from mice provided by Danijela Vignjevic (Insitut Curie, Paris) [54]. Myosin-IIA-GFP-knock-in mice [55] were provided by Robert S. Adelstein (NHLBI, Bethesda) and Ana-Maria Lennon-Dumesnil (Institut Curie, Paris). Myosin-IIA-KO/mTmG mice were kindly provided by Danijela Vignjevic (Institut Curie, Paris) [54,56]. Cre recombinase for Myosin-IIA-KO was induced with 100nM of 4-hydroxytamoxifen for 24h (#SML1666, Sigma-Aldrich).

METHOD DETAILS

Organoid preparation

6 to 12 weeks-old mice were used for organoid generation. After euthanization by cervical dislocation, the small intestine was harvested, flushed with PBS to discard luminal content and cut longitudinally open. The tissue was then cut into small pieces of 3-5 mm and further washed in PBS.

For organoid preparation, the pieces of intestinal tissue were then incubated on ice for 10 min in a tube containing 5 mM EDTA. The tube was then vortexed for 2 min to release villi from the tissue. After EDTA removal, the intestinal pieces were placed in cold PBS and vortexed vigorously for 3 min to ensure crypt release. This process was repeated 3 times, with each fraction recovered. The third and fourth fractions are usually concentrated in crypts, so these are combined and passed through a 70-µm cell strainer to remove remaining villi and centrifuged at 1000 RPM for 5 min. The pellet (crypts) was then washed in advanced DMEM/F12 (#12634010 Thermo Fisher Scientific, Waltham, Massachusetts, USA) and centrifuged. The final pellet is resuspended in 50 µl of 1:1 ratio of advanced DMEM/F12 and ice-cold Matrigel (#734-1100 VWR, Radnor, PA, USA) and plated as domes. Incubation at 37°C for 20-30 min allowed Matrigel polymerization. 3D organoid culture was performed in IntestiCult™ Organoid Growth medium (#06005 StemCell Technologies, Vancouver, Canada), from here on termed ENR medium. Organoid stocks were routinely grown in Matrigel with IntestiCult™ Organoid Growth medium and passaged every 7 to 10 days. Medium was changed every 2 days.

For 2D organoid monolayer preparation, 3D organoids were cultured in L-WRN conditioned media for at least 3 days before use. Organoids were harvested with cold advanced DMEM/F12 and transferred in a falcon tube. Organoids were mechanically broken through a P200-filtered tip 150 times. The solution of broken organoids was centrifuged at 72g for 3 mins at 4°C. The supernatant was removed and 5 mL of fresh F12 was added. The breaking step and centrifugation were repeated once. Then the cell pellet was filtered through a 30 µm cell strainer. The pellet was resuspended in warm L-WRN conditioned media + 10µM Y27632 (StemCell #72302) and 150 µL of were gently seeded on the crosslinked Matrigel substrate (18 mm coated coverslips on a 12 well plate) making sure the solution stays on the coverslip. After 4h of incubation in a 37°C incubator, more L-WRN conditioned media + 10 µM Y27632 (up to 1 mL/well) were added for the first 24h culture. After 24h, cells were subsequently grown on L-WRN conditioned media (without Y27632). Culture media were replaced every 24-48 hours with fresh L-WRN conditioned media and the organoid-derived monolayers were cultured for 10 days before immunostaining or live imaging.

Preparation of L-WRN conditioned medium

The L-WRN conditioned media was prepared from L-WRN cells, acquired from ATCC (ATCC CRL-3276), according to Miyoshi and Stappenbeck [57]. L-WRN cells were cultured in L-Cell

817 medium (DMEM high glucose (Sigma-Aldrich, cat. no. D6429) supplemented with FBS (10%
818 v/v), Glutamax (2 mM) and penicillin/streptomycin (100 units/mL). After the first day, selection
819 media was added, containing Geneticin (500 µg/mL) and hygromycin (500 µg/mL). Once
820 confluent cells were passed into five T175 flask and cultured in L-cells media until confluency.
821 Then cells were cultured in Primary Cells Medium (PCM) (Advanced DMEM/F12
822 supplemented with FBS (20% v/v), Glutamax (2 mM) and penicillin/streptmycin (100 units/mL).
823 The PCM supplemented with Wnt-3a, R-spondin and Noggin secreted by the L-WRN cells
824 was collected every 24h and mixed with freshly made PCM at a 1:1 ratio and was vacuum
825 filtered through 0.22 µm membrane membrane to make EM.
826
827 **Human biopsies and preparation of tissue samples**
828 Tissue samples of human duodenum were provided by Necker-Enfants Malades Hospital
829 (Paris, France) and were collected from the Necker Paediatric Anatomo-Pathology
830 Department for retrospective analyses. The biopsies analyzed here comprised 1 patient with
831 gastralgia, 1 patient with anemia, and 1 patient with coeliac disease under gluten-free diet.
832 Duodenal biopsies were collected during endoscopic procedures for diagnosis and/or
833 monitoring of patients. All parents signed informed consent forms approved by the local ethics
834 committee for biopsy exploitation (Unité de Recherche Clinique (URC) of Necker Hospital,
835 URC). For immunohistochemical analyses, biopsies were fixed for 2 h in 4% formaldehyde.
836 The samples were then paraffin embedded. 5 µm sections were de-waxed in a xylene bath,
837 rehydrated in isopropanol and in solutions with decreasing ethanol concentrations, and were
838 processed for immunostaining. De-waxed tissue sections were blocked in 1.5% donkey serum
839 (Sigma-Aldrich, St Louis, Missouri, USA) for 1 h. Primary antibody incubations were performed
840 at 4°C overnight and secondary antibody incubations at room temperature for 2 h, both in
841 1.5% donkey serum solution. Hoechst 33342 staining (Life Technologies, Paisley, UK) was
842 used to detect nuclei. Tissue sections were mounted in home-made Mowiol 488 solution.
843
844 ***Caco2 cell culture***
845 Caco2 cells, originally acquired from ATCC, were kindly provided by Dr. S. Robine (Curie
846 Institute, Paris). Caco2 cells were routinely grown in DMEM 4.5 g/l glucose supplemented with
847 20% fetal bovine serum and 1% penicillin-streptomycin (Gibco, Thermo Fischer Scientific,
848 Waltham, MA, USA) for a maximum of 9 passages. The culture medium was renewed every
849 2-days.
850
851 ***Cross-linked Matrigel substrates (CL-Matrigel)***
852 To produce cross-linked Matrigel (CL-Matrigel) substrates, a fresh-made cross-linker solution
853 was prepared by mixing 100 mM NHS (Sigma-Aldrich) and 400 mM EDC (Sigma-Aldrich) in

cold PBS 4°C. Glass coverslips (Ø = 18 mm) were plasma treated and then were cooled in a fridge (-20°C, 3 min). Cross-linker solution then was mixed well with thawed pure Matrigel at a ratio of 1:10 (v/v) and 50µL drops of the mixture were then poured on top of the cooled plasma treated coverslip and were spread by tilting the coverslips. Subsequently, the coverslips were placed in a 37°C incubator in a 12 well plate for 2h to form CL-Matrigel layers. While incubation, PBS were poured in 2 empty wells of the 12 well plate ware to prevent gel dehydration. The CL-Matrigel substrates were washed with PBS once and incubated in PBS at 37°C for 24 h to remove unreacted EDC and NHS. The substrates can be stored up to a week in incubator 1X PBS for future utilization. Before use, the coverslips were washed 2 times with 1X PBS.

Glass coverslip micropatterning with deep UV and cell seeding

The micropatterning protocol was adapted from [58]. For polystyrene coating, 20x20 glass coverslips (1304369, Schott) were cleaned for 10min in acetone then for 10min in isopropanol in a bath sonicator and then dried with compressed-clean air under a laminar flow hood. They were first coated with adhesion promoter Ti-Prime (MicroChemicals) using a spin-coater (WS-650m2-23NPPB, Laurell) at 3000 rpm for 30s and baked on top heater for 2min at 120°C. Then a 1% polystyrene (MW 260,000, 178891000, Acros Organic) solution in toluene (179418, Sigma-Aldrich) was spin-coated on the coverslip at 1000 rpm.

For coverslip passivation, polystyrene layer was oxidized by exposure to air-plasma as described above and immersed into a solution of poly(L-lysine)-graft-poly(ethylene glycol) (PLL-g-PEG) (ZZ241PO22, JenKem Technology, Beijing) at 0.1 mg/mL in HEPES (10mM, pH 7.4) for 1 hour at room temperature. Coverslips were then washed in HEPES buffer and air dried.

For coverslip micropatterning, passivated coverslips were put in tight contact with a chromed etched photomask (Toppan Photomask). Tight contact was maintained using a homemade vacuum holder. The PLL-PEG layer was burned with deep UV (λ=190nm) through the etched windows of the photomask, using UVO cleaner (Model No. 342A-220, Jelight), at a distance of 1cm from the UV lamp with a power of 6mW/cm2, for 3 min. Exposed coverslips were then incubated with a solution of 10µg/ml fibronectin (F1141, Sigma) in carbonate buffer (100 mM $NaHCO_3$ buffer, pH 8.5) for 30min at room temperature. Micropatterned coverslips were then washed with the carbonate buffer. Caco2 cells were directly seeded on these micropatterned coverslips on a 35 mm petri dish and were grown for 4 – 5 days.

Immunostaining

Routinely, organoid-derived monolayers were fixed using 4% paraformaldehyde for 30 min, then permeabilized using 0.1% triton-x-100 in PBS for 10-15 min. The blocking step was

performed in 4% goat serum /1% BSA solution for 1 hour, before proceeding to incubation with primary antibody at 4°C overnight. The next day, the primary antibody was removed and the monolayers were washed 3 times in PBS for 10 min each, before adding the secondary antibody and left to incubate for 2h at room temperature. Finally, monolayers were washed 3 times again for 10 minutes before incubating in Hoechst 33342 for 15 min to stain nuclei. Immunostained samples were mounted in homemade Mowiol solution. For F-actin staining, fluorescently labelled phalloidin was added during secondary antibody incubation.

For immunostaining of *in vivo* mouse intestine, 1-mm pieces of mouse jejunum were fixed in 4% PFA overnight under shaking for 1 hour. After PBS wash, tissue permeabilization was performed in 1% Triton X-100 / PBS solution for 1 h, before blocking in 1% BSA / 4% goat serum / 0.2% Triton X-100 / PBS solution for 1 h. Incubations with primary and secondary antibodies were done in 0.1% BSA / 0.3 % goat serum / 0.2 % Triton X-100 / PBS overnight at 4°C. Hoechst33342 staining was used to detect nuclei. Immunostained samples were mounted in Vectashield (Vector Laboratories, Burlingame, CA).

Antibodies and reagents

Mouse monoclonal antibody directed against X (clone X, IF dilution, 1:100) was purchased from Sigma-Aldrich. Mouse monoclonal antibody directed against E-cadherin (clone 36, #610181, IF dilution, 1:50) was from BD Biosciences. Rabbit polyclonal antibody directed against Phospho-Myosin Light Chain 2 (Ser19, #3671, IF dilution, 1:100) and rabbit monoclonal antibody directed against E-cadherin (clone 24E10, #3195S, IF dilution 1:100) were from Cell Signaling Technology. Rabbit polyclonal antibody directed against non-muscle myosin heavy chain II-A antibody (clone poly19098, #909801, WB dilution 1:500) was from Biolegend. Goat anti-mouse-Alexa-488, 568, anti-rabbit-Alexa488, 568 or 647 were from Life Technologies (Paisley, UK). Nuclei were stained with Hoechst 33342 solution incubation (Life Technologies) at a 1:1000 dilution. Blebbistatin, Y-27632 and nocodazole were from Sigma Aldrich (Saint-Louis, MO, USA). CellMask Actin Deep Red actin tracking stain (#A57245) was from Invitrogen (Thermo Fisher Scientific). Azidoblebbistatin (#MPH-198) was from MotorPharma (Budapest, Hungary).

Drug treatments

Organoids were incubated in 10μM blebbistatin for 1.5h, then washed out with PBS and prepared for immunostaining or live-imaging. Cells were incubated for 1.5h in DMSO as controls. For live blebbistatin photo-activation organoid derived monolayer were first stained with CellMask actin GFP and then were incubated with 10μM azidoblebbistatin (Cat#DR-A-081, Motor pharma) or DMSO controls for 1h. The samples were then was taken for live imaging in a LSM 980 scanning probe microscope equipped with a multiphoton setup.

928 Azidoblebbistatin was photoactivated in the selected ROI using a 2-photon 800 nm laser
929 irradiation [59] and live images were acquired.
930
931 ***Laser ablation experiments***
932 For Laser ablation experiments, F-actin was first labelled in live organoid-derived monolayers
933 by incubating with CellMask™ Green Actin Tracking stain (Invitrogen) for 1 hour in culture
934 media. Labelled monolayer was then taken in a live imaging setup on a spinning disc confocal
935 microscope (CSU-XI) equipped with laser ablation setup. The ablation was done using a
936 pulsed 355 nm UV at a power of 25% using an iLas system (Roper Scientific) in Metamorph
937 and images were obtained using a 40x or 100X oil objective. Node displacement was manually
938 tracked using TrackMate in imageJ.
939
940 ***Live imaging***
941 Dynamics experiments on live organoid-derived monolayers were performed on a live imaging
942 setup on an inverted Zeiss microscope equipped with a CSU-X1 spinning disk head
943 (Yokogawa – Andor), using Zeiss 40X and 63X objectives.
944
945 ***Segmentation and analyses***
946 Segmentation - We used CellPose 2.0 (https://www.cellpose.org/; [60]) to perform cell
947 segmentation. Mask dilatation was used to extract the cell contours and location of tricellular
948 junctions, called vertices.
949
950 Hexatic order analysis**-** For each cell (indexed by $J = 1,2,3,\cdots,N$ with N the total number of
951 cells), we define a hexatic order parameter value:

952 $$\psi_{6,J} = \frac{1}{N_J} \sum_{K \in neighbors} exp\ (i6\theta_{JK}),$$

953 where $\theta_{JK} = arg\ (r_K - r_J)$, is the angle between the considered cell center, denoted r_J, and
954 the one of its neighbour, r_K; N_J is the number of neighbor cells of the J-th cell. The overall
955 hexatic order is then defined as $\psi_6 = \frac{|\sum_{J=1}^{N} \psi_{6,J}|}{N}$.

956 Triangular order We define a triangular order parameter value:

957 $$\psi_{3,i} = \frac{1}{3} \sum_{j \in neighbors} exp\ (i3\theta_{ij}),$$

where $\theta_{ij} = arg\ (r_j - r_i)$, is the angle of the cell-cell junction ij. The overall triangular order is then defined as $\psi_3 = \sum_{i=1}^{N_v} \frac{|\psi_{3,i}|}{N_v}$.

Strain For each detected cells, we estimate a cell shape tensor Λ whose *xx* components read:

$$\Lambda_{xx} = \sum_{n \in bounday} (x_n - x^-)^2$$

where (x_n, y_n) is the coordinate of the boundary pixels n and $(x^-, y^-) = \sum_n \frac{(x_n, y_n)}{n}$ is the cell barycenter; the xy and yy components are defined similarly. The matrix Λ has positive eigenvalues Λ_1 and Λ_2 with $\Lambda_1 \geq \Lambda_2$. We then define the cellular strain as:

$$\varepsilon_{el} = \frac{1}{2} log\ (\frac{\Lambda_1}{\Lambda_2})$$

In the strain quantification, we exclude detected objects with an area smaller than 2 microns.

Tracking We used StarDist in TrackMate (FiJi [61]) for cell tracking analyses. We used a Kalman tracker parameterized with a search radius of approximately half the cell typical size, an initial search radius 10% higher, and a maximum frame gap of 2 [62,63].

Velocity Correlation Functions For every cells, with position r_i, we compute the velocity autocorrelation function:

$$C_t(\tau) = C(r_i, t) = v(r_i, t) \cdot v \frac{(r_i, t + \tau)}{|v(r_i, t)|^2},$$

where τ is the delay time. We also evaluate the spatial velocity correlation function:

$$C_s(r) = C(r, t) = v(r_i, t) \cdot v \frac{(r_i + r, t)}{|v(r_i, t)|^2},$$

where $r = r_j - r_i$ and r_j is the position of the cell j. For each experiment, we estimate the average correlation function $\langle C_s(r) \rangle$ over all tracks and all times (see Figure 7E-J in the main text).

Practically, in our evaluation of the velocity functions, we discarded every track which was shorter than 4 frames.

Computational model

We employed a cell-based computational model, called the vertex model [64,65,66], to simulate the multicellular response of cell differentiation, cell ablation, and contractility recovery of multicellular actin star network. In this model, the cell monolayer is represented as a tiling of polygons, see Figure 6D. The dynamics of cells are determined by force balance equations at each vertex:

$$F_i^{(friction)} + F_i^{(viscous)} + F_i^{(elastic)} + F_i^{(active)} = 0$$

where (1) $F_i^{(friction)} = -\xi v_i$ is the friction force between the monolayer and the substrate, with ξ being the friction coefficient and $v_i = d\frac{r_i}{dt}$ being the velocity of the vertex i. (2) $F_i^{(viscous)} = \eta \sum_j C_{ij} \cdot v_j$ is the viscous force at vertex i, which depends on the velocities of the neighbor vertices j and scales proportionally to a viscous modulus η that models dissipation along the cell-cell junction and within the bulk cytoplasm; C_{ij} is a viscous structure tensor that depends on the vertices' positions (r_i), and the topological relation of cells and vertices [67] (see Supplementary Information); (3) $F_i^{(elastic)}$ is the elastic force stemming from variations in the cell shape, classically expressed as $F_i^{(elastic)} = -\partial \frac{E}{\partial} r_i$ with [65,68,67,69,70] :

$$E = \sum_{J=1}^{N} \frac{1}{2} K_A (A_J - A_0)^2 + \sum_{J=1}^{N} \frac{1}{2} K_P (P_J - P_0)^2,$$

where K_A and K_P are the rigidities associated with cell area and cell perimeter; A_0 and P_0 are the preferred cell area and the preferred cell perimeter, respectively; A_J and P_J are the actual area and perimeter of the J-th cell, respectively. (4) the active force $F_i^{(active)}$ corresponds to the forces induced by the multicellular actin star network; we decompose the actin star network into two contributions, resulting from: (4.1) an active pulling stress $\sigma_J^{(active,\perp)} = \alpha_J I$ with $\alpha_J \geq 0$ quantifies the intensity of the active pulling stress induced by the contractility of the actin star network within the J-th cell, which describes the active pulling force normal to cell edges, see Supplementary Information, Figure S1; and (4.2) an active tension $\chi_J > 0$ parallel to edges of the J-th cell, see Supplementary Information, Figure S1. We show that the active pulling stress α_J and the active tension χ_J are equivalent to renormalizing E into E_{eff} with a renormalized target area $A_{0,J} = A_0 - \frac{\alpha_J}{K_A}$ and a renormalized target perimeter $P_{0,J} = P_0 - \frac{\chi_J}{(2K_P)}$ (see Supplementary Materials). Consequently, we obtain the following dynamic equation on the velocities:

$$-\xi v_i + \sum_j \eta\, C_{ij} \cdot v_j = \frac{\partial E_{eff}}{\partial r_i}$$

We then solve the latter equation to estimate the vertex displacement at each simulation time step. Last, we mention that in the laser ablation simulations, the cells at the k-th row are defined by the distance d of the cell centre to the ablation site if it satisfies k-1/2 < d/L_{cell} < k+1/2 with L_{cell} = 10 μm being the cell size.

Statistical analysis

All statistical analyses were performed using Prism (GraphPad Software, San Diego, CA, USA, version 9.0). Statistical details of experiments can be found in the figure legends. Unless otherwise stated, experiments were replicated 3 times independently.

REFERENCES

1. Lecuit, T., Lenne, P.F., and Munro, E. (2011). Force generation, transmission, and integration during cell and tissue morphogenesis. Annu Rev Cell Dev Biol *27*, 157-184. 10.1146/annurev-cellbio-100109-104027.
2. Levayer, R., and Lecuit, T. (2013). Oscillation and polarity of E-cadherin asymmetries control actomyosin flow patterns during morphogenesis. Dev Cell *26*, 162-175. 10.1016/j.devcel.2013.06.020.
3. Sanchez-Corrales, Y.E., and Roper, K. (2018). Alignment of cytoskeletal structures across cell boundaries generates tissue cohesion during organ formation. Curr Opin Cell Biol *55*, 104-110. 10.1016/j.ceb.2018.07.001.
4. Vicente-Manzanares, M., Ma, X., Adelstein, R.S., and Horwitz, A.R. (2009). Non-muscle myosin II takes centre stage in cell adhesion and migration. Nat Rev Mol Cell Biol *10*, 778-790. 10.1038/nrm2786.
5. McCaffrey, L.M., and Macara, I.G. (2011). Epithelial organization, cell polarity and tumorigenesis. Trends Cell Biol *21*, 727-735. 10.1016/j.tcb.2011.06.005.
6. Buckley, C.E., and St Johnston, D. (2022). Apical-basal polarity and the control of epithelial form and function. Nat Rev Mol Cell Biol *23*, 559-577. 10.1038/s41580-022-00465-y.
7. Thompson, D.W. (1942). On growth and form. Macmillian, Cambridge University Press.
8. Pickett, M.A., Naturale, V.F., and Feldman, J.L. (2019). A Polarizing Issue: Diversity in the Mechanisms Underlying Apico-Basolateral Polarization In Vivo. Annu Rev Cell Dev Biol *35*, 285-308. 10.1146/annurev-cellbio-100818-125134.
9. Furukawa, K.T., Yamashita, K., Sakurai, N., and Ohno, S. (2017). The Epithelial Circumferential Actin Belt Regulates YAP/TAZ through Nucleocytoplasmic Shuttling of Merlin. Cell Rep *20*, 1435-1447. 10.1016/j.celrep.2017.07.032.
10. Tepass, U., Truong, K., Godt, D., Ikura, M., and Peifer, M. (2000). Cadherins in embryonic and neural morphogenesis. Nat Rev Mol Cell Biol *1*, 91-100. 10.1038/35040042.
11. Campas, O., Noordstra, I., and Yap, A.S. (2023). Adherens junctions as molecular regulators of emergent tissue mechanics. Nat Rev Mol Cell Biol. 10.1038/s41580-023-00688-7.
12. Guillot, C., and Lecuit, T. (2013). Mechanics of epithelial tissue homeostasis and morphogenesis. Science *340*, 1185-1189. 10.1126/science.1235249.
13. Heisenberg, C.P., and Bellaiche, Y. (2013). Forces in tissue morphogenesis and patterning. Cell *153*, 948-962. 10.1016/j.cell.2013.05.008.
14. Martin, A.C., Kaschube, M., and Wieschaus, E.F. (2009). Pulsed contractions of an actin-myosin network drive apical constriction. Nature *457*, 495-499. 10.1038/nature07522.
15. Rauzi, M., Lenne, P.F., and Lecuit, T. (2010). Planar polarized actomyosin contractile flows control epithelial junction remodelling. Nature *468*, 1110-1114. 10.1038/nature09566.
16. Jodoin, J.N., Coravos, J.S., Chanet, S., Vasquez, C.G., Tworoger, M., Kingston, E.R., Perkins, L.A., Perrimon, N., and Martin, A.C. (2015). Stable Force Balance between Epithelial Cells Arises from F-Actin Turnover. Dev Cell *35*, 685-697. 10.1016/j.devcel.2015.11.018.
17. Coravos, J.S., and Martin, A.C. (2016). Apical Sarcomere-like Actomyosin Contracts Nonmuscle Drosophila Epithelial Cells. Dev Cell *39*, 346-358. 10.1016/j.devcel.2016.09.023.
18. Bailles, A., Collinet, C., Philippe, J.M., Lenne, P.F., Munro, E., and Lecuit, T. (2019). Genetic induction and mechanochemical propagation of a morphogenetic wave. Nature *572*, 467-473. 10.1038/s41586-019-1492-9.

19. Keller, R. (2006). Mechanisms of elongation in embryogenesis. Development *133*, 2291-2302. 10.1242/dev.02406.
20. Lawson-Keister, E., and Manning, M.L. (2021). Jamming and arrest of cell motion in biological tissues. Curr Opin Cell Biol *72*, 146-155. 10.1016/j.ceb.2021.07.011.
21. Xi, W., Saleh, J., Yamada, A., Tomba, C., Mercier, B., Janel, S., Dang, T., Soleilhac, M., Djemat, A., Wu, H., et al. (2022). Modulation of designer biomimetic matrices for optimized differentiated intestinal epithelial cultures. Biomaterials *282*, 121380. 10.1016/j.biomaterials.2022.121380.
22. Thorne, C.A., Chen, I.W., Sanman, L.E., Cobb, M.H., Wu, L.F., and Altschuler, S.J. (2018). Enteroid Monolayers Reveal an Autonomous WNT and BMP Circuit Controlling Intestinal Epithelial Growth and Organization. Dev Cell *44*, 624-633 e624. 10.1016/j.devcel.2018.01.024.
23. Perez-Gonzalez, C., Ceada, G., Greco, F., Matejcic, M., Gomez-Gonzalez, M., Castro, N., Menendez, A., Kale, S., Krndija, D., Clark, A.G., et al. (2021). Mechanical compartmentalization of the intestinal organoid enables crypt folding and collective cell migration. Nat Cell Biol *23*, 745-757. 10.1038/s41556-021-00699-6.
24. Murrell, M.P., and Gardel, M.L. (2012). F-actin buckling coordinates contractility and severing in a biomimetic actomyosin cortex. Proc Natl Acad Sci U S A *109*, 20820-20825. 10.1073/pnas.1214753109.
25. Sonal, Ganzinger, K.A., Vogel, S.K., Mucksch, J., Blumhardt, P., and Schwille, P. (2018). Myosin-II activity generates a dynamic steady state with continuous actin turnover in a minimal actin cortex. J Cell Sci *132*. 10.1242/jcs.219899.
26. Tse, J.R., and Engler, A.J. (2010). Preparation of hydrogel substrates with tunable mechanical properties. Curr Protoc Cell Biol *Chapter 10*, Unit 10 16. 10.1002/0471143030.cb1016s47.
27. Henkes, S., Kostanjevec, K., Collinson, J.M., Sknepnek, R., and Bertin, E. (2020). Dense active matter model of motion patterns in confluent cell monolayers. Nat Commun *11*, 1405. 10.1038/s41467-020-15164-5.
28. Iskratsch, T., Wolfenson, H., and Sheetz, M.P. (2014). Appreciating force and shape-the rise of mechanotransduction in cell biology. Nat Rev Mol Cell Biol *15*, 825-833. 10.1038/nrm3903.
29. Wolfenson, H., Yang, B., and Sheetz, M.P. (2019). Steps in Mechanotransduction Pathways that Control Cell Morphology. Annu Rev Physiol *81*, 585-605. 10.1146/annurev-physiol-021317-121245.
30. Lappalainen, P., Kotila, T., Jegou, A., and Romet-Lemonne, G. (2022). Biochemical and mechanical regulation of actin dynamics. Nat Rev Mol Cell Biol *23*, 836-852. 10.1038/s41580-022-00508-4.
31. Lazarides, E. (1976). Actin, alpha-actinin, and tropomyosin interaction in the structural organization of actin filaments in nonmuscle cells. J Cell Biol *68*, 202-219. 10.1083/jcb.68.2.202.
32. Duffy, L., and O'Reilly, S. (2018). Functional Implications of Cross-Linked Actin Networks in Trabecular Meshwork Cells. Cell Physiol Biochem *45*, 783-794. 10.1159/000487170.
33. Peng, M., Rayana, N.P., Dai, J., Sugali, C.K., Baidouri, H., Suresh, A., Raghunathan, V.K., and Mao, W. (2022). Cross-linked actin networks (CLANs) affect stiffness and/or actin dynamics in transgenic transformed and primary human trabecular meshwork cells. Exp Eye Res *220*, 109097. 10.1016/j.exer.2022.109097.
34. Xia, S., Lim, Y.B., Zhang, Z., Wang, Y., Zhang, S., Lim, C.T., Yim, E.K.F., and Kanchanawong, P. (2019). Nanoscale Architecture of the Cortical Actin Cytoskeleton in Embryonic Stem Cells. Cell Rep *28*, 1251-1267 e1257. 10.1016/j.celrep.2019.06.089.
35. Luo, W., Yu, C.H., Lieu, Z.Z., Allard, J., Mogilner, A., Sheetz, M.P., and Bershadsky, A.D. (2013). Analysis of the local organization and dynamics of cellular actin networks. J Cell Biol *202*, 1057-1073. 10.1083/jcb.201210123.

36. Vogel, S.K., Heinemann, F., Chwastek, G., and Schwille, P. (2013). The design of MACs (minimal actin cortices). Cytoskeleton (Hoboken) *70*, 706-717. 10.1002/cm.21136.
37. Muresan, C.G., Sun, Z.G., Yadav, V., Tabatabai, A.P., Lanier, L., Kim, J.H., Kim, T., and Murrell, M.P. (2022). F-actin architecture determines constraints on myosin thick filament motion. Nat Commun *13*, 7008. 10.1038/s41467-022-34715-6.
38. Putra, V.D.L., Kilian, K.A., and Knothe Tate, M.L. (2023). Biomechanical, biophysical and biochemical modulators of cytoskeletal remodelling and emergent stem cell lineage commitment. Commun Biol *6*, 75. 10.1038/s42003-022-04320-w.
39. Humphrey, J.D., Dufresne, E.R., and Schwartz, M.A. (2014). Mechanotransduction and extracellular matrix homeostasis. Nat Rev Mol Cell Biol *15*, 802-812. 10.1038/nrm3896.
40. Paluch, E.K., Nelson, C.M., Biais, N., Fabry, B., Moeller, J., Pruitt, B.L., Wollnik, C., Kudryasheva, G., Rehfeldt, F., and Federle, W. (2015). Mechanotransduction: use the force(s). BMC Biol *13*, 47. 10.1186/s12915-015-0150-4.
41. Elosegui-Artola, A., Trepat, X., and Roca-Cusachs, P. (2018). Control of Mechanotransduction by Molecular Clutch Dynamics. Trends Cell Biol *28*, 356-367. 10.1016/j.tcb.2018.01.008.
42. Sumigray, K.D., Terwilliger, M., and Lechler, T. (2018). Morphogenesis and Compartmentalization of the Intestinal Crypt. Dev Cell *45*, 183-197 e185. 10.1016/j.devcel.2018.03.024.
43. Hartl, L., Huelsz-Prince, G., van Zon, J., and Tans, S.J. (2019). Apical constriction is necessary for crypt formation in small intestinal organoids. Dev Biol *450*, 76-81. 10.1016/j.ydbio.2019.03.009.
44. Yang, Q., Xue, S.L., Chan, C.J., Rempfler, M., Vischi, D., Maurer-Gutierrez, F., Hiiragi, T., Hannezo, E., and Liberali, P. (2021). Cell fate coordinates mechano-osmotic forces in intestinal crypt formation. Nat Cell Biol *23*, 733-744. 10.1038/s41556-021-00700-2.
45. Barker, N. (2014). Adult intestinal stem cells: critical drivers of epithelial homeostasis and regeneration. Nat Rev Mol Cell Biol *15*, 19-33. 10.1038/nrm3721.
46. Delacour, D., Salomon, J., Robine, S., and Louvard, D. (2016). Plasticity of the brush border - the yin and yang of intestinal homeostasis. Nat Rev Gastroenterol Hepatol. 10.1038/nrgastro.2016.5.
47. Keller, T.C., 3rd, Conzelman, K.A., Chasan, R., and Mooseker, M.S. (1985). Role of myosin in terminal web contraction in isolated intestinal epithelial brush borders. J Cell Biol *100*, 1647-1655.
48. Meenderink, L.M., Gaeta, I.M., Postema, M.M., Cencer, C.S., Chinowsky, C.R., Krystofiak, E.S., Millis, B.A., and Tyska, M.J. (2019). Actin Dynamics Drive Microvillar Motility and Clustering during Brush Border Assembly. Dev Cell *50*, 545-556 e544. 10.1016/j.devcel.2019.07.008.
49. De Ceccatty, M.P. (1986). Cytoskeletal organization and tissue patterns of epithelia in the sponge Ephydatia mulleri. J Morphol *189*, 45-65. 10.1002/jmor.1051890105.
50. Kroeger, B., Manning, S.A., Fonseka, Y., Oorschot, V., Crawford, S.A., Ramm, G., and Harvey, K.F. (2024). Basal spot junctions of Drosophila epithelial tissues respond to morphogenetic forces and regulate Hippo signaling. Dev Cell *59*, 262-279 e266. 10.1016/j.devcel.2023.11.024.
51. Efimova, N., and Svitkina, T.M. (2018). Branched actin networks push against each other at adherens junctions to maintain cell-cell adhesion. J Cell Biol *217*, 1827-1845. 10.1083/jcb.201708103.
52. Pasupalak, A., Yan-Wei, L., Ni, R., and Pica Ciamarra, M. (2020). Hexatic phase in a model of active biological tissues. Soft Matter *16*, 3914-3920. 10.1039/d0sm00109k.
53. Snippert, H.J., van der Flier, L.G., Sato, T., van Es, J.H., van den Born, M., Kroon-Veenboer, C., Barker, N., Klein, A.M., van Rheenen, J., Simons, B.D., and Clevers, H. (2010). Intestinal crypt homeostasis results from neutral competition between symmetrically dividing Lgr5 stem cells. Cell *143*, 134-144. 10.1016/j.cell.2010.09.016.

54. Krndija, D., El Marjou, F., Guirao, B., Richon, S., Leroy, O., Bellaiche, Y., Hannezo, E., and Matic Vignjevic, D. (2019). Active cell migration is critical for steady-state epithelial turnover in the gut. Science *365*, 705-710. 10.1126/science.aau3429.
55. Zhang, Y., Conti, M.A., Malide, D., Dong, F., Wang, A., Shmist, Y.A., Liu, C., Zerfas, P., Daniels, M.P., Chan, C.C., et al. (2012). Mouse models of MYH9-related disease: mutations in nonmuscle myosin II-A. Blood *119*, 238-250. 10.1182/blood-2011-06-358853.
56. Saleh, J., Fardin, M.A., Barai, A., Soleilhac, M., Frenoy, O., Gaston, C., Cui, H., Dang, T., Gaudin, N., Vincent, A., et al. (2023). Length limitation of astral microtubules orients cell divisions in murine intestinal crypts. Dev Cell *58*, 1519-1533 e1516. 10.1016/j.devcel.2023.06.004.
57. Miyoshi, H., and Stappenbeck, T.S. (2013). In vitro expansion and genetic modification of gastrointestinal stem cells in spheroid culture. Nat Protoc *8*, 2471-2482. 10.1038/nprot.2013.153.
58. Azioune, A., Carpi, N., Tseng, Q., Thery, M., and Piel, M. (2010). Protein micropatterns: A direct printing protocol using deep UVs. Methods Cell Biol *97*, 133-146. 10.1016/S0091-679X(10)97008-8.
59. Kepiro, M., Varkuti, B.H., Bodor, A., Hegyi, G., Drahos, L., Kovacs, M., and Malnasi-Csizmadia, A. (2012). Azidoblebbistatin, a photoreactive myosin inhibitor. Proc Natl Acad Sci U S A *109*, 9402-9407. 10.1073/pnas.1202786109.
60. Pachitariu, M., and Stringer, C. (2022). Cellpose 2.0: how to train your own model. Nat Methods *19*, 1634-1641. 10.1038/s41592-022-01663-4.
61. Schindelin, J., Arganda-Carreras, I., Frise, E., Kaynig, V., Longair, M., Pietzsch, T., Preibisch, S., Rueden, C., Saalfeld, S., Schmid, B., et al. (2012). Fiji: an open-source platform for biological-image analysis. Nat Methods *9*, 676-682. 10.1038/nmeth.2019.
62. Ershov, D., Phan, M.S., Pylvanainen, J.W., Rigaud, S.U., Le Blanc, L., Charles-Orszag, A., Conway, J.R.W., Laine, R.F., Roy, N.H., Bonazzi, D., et al. (2022). TrackMate 7: integrating state-of-the-art segmentation algorithms into tracking pipelines. Nat Methods *19*, 829-832. 10.1038/s41592-022-01507-1.
63. Schmidt U, W.M., Broaddus C and Myers G (2018). Cell detection with star-convex polygons. Medical image computing and computer assisted intervention, 265-273. doi.org/10.1007/978-3-030-00934-2_30.
64. H, N.T.a.H. (2001). A dynamic cell model for the formation of epithelial tissues. Philosophical magazine B *81*, 699-719.
65. Farhadifar, R., Roper, J.C., Aigouy, B., Eaton, S., and Julicher, F. (2007). The influence of cell mechanics, cell-cell interactions, and proliferation on epithelial packing. Curr Biol *17*, 2095-2104. 10.1016/j.cub.2007.11.049.
66. Alt, S., Ganguly, P., and Salbreux, G. (2017). Vertex models: from cell mechanics to tissue morphogenesis. Philos Trans R Soc Lond B Biol Sci *372*. 10.1098/rstb.2015.0520.
67. Bi D, L.J., Schwarz JM and Manning ML (2015). A density-independent rigidity transition in biological tissues. Nature Physics *11*, 1074-1074.
68. Fletcher, A.G., Osterfield, M., Baker, R.E., and Shvartsman, S.Y. (2014). Vertex models of epithelial morphogenesis. Biophys J *106*, 2291-2304. 10.1016/j.bpj.2013.11.4498.
69. Lin, S.Z., Ye, S., Xu, G.K., Li, B., and Feng, X.Q. (2018). Dynamic Migration Modes of Collective Cells. Biophys J *115*, 1826-1835. 10.1016/j.bpj.2018.09.010.
70. Lin, S.Z., Merkel, M., and Rupprecht, J.F. (2023). Structure and Rheology in Vertex Models under Cell-Shape-Dependent Active Stresses. Phys Rev Lett *130*, 058202. 10.1103/PhysRevLett.130.058202.

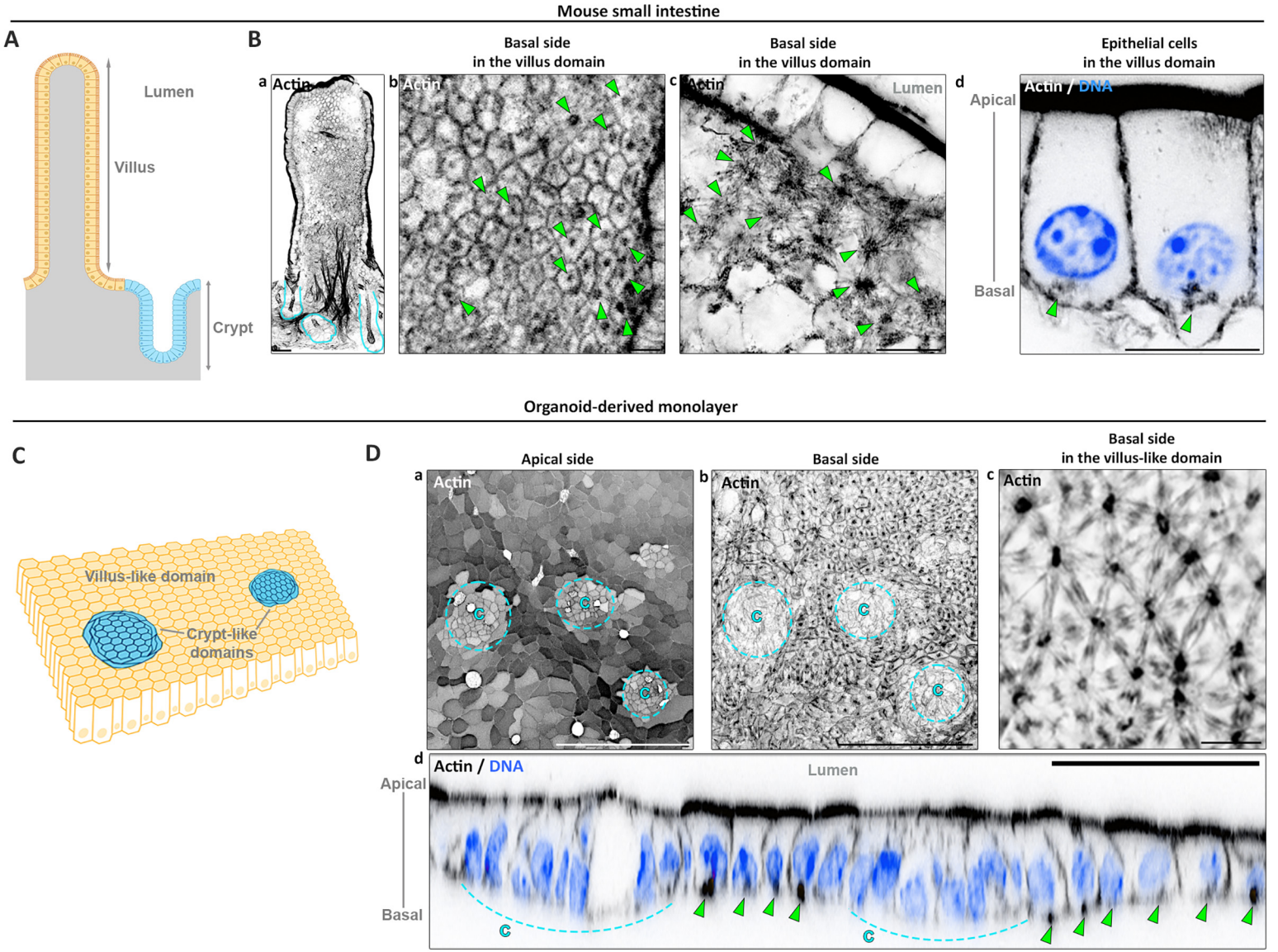

Barai et al., Figure 1

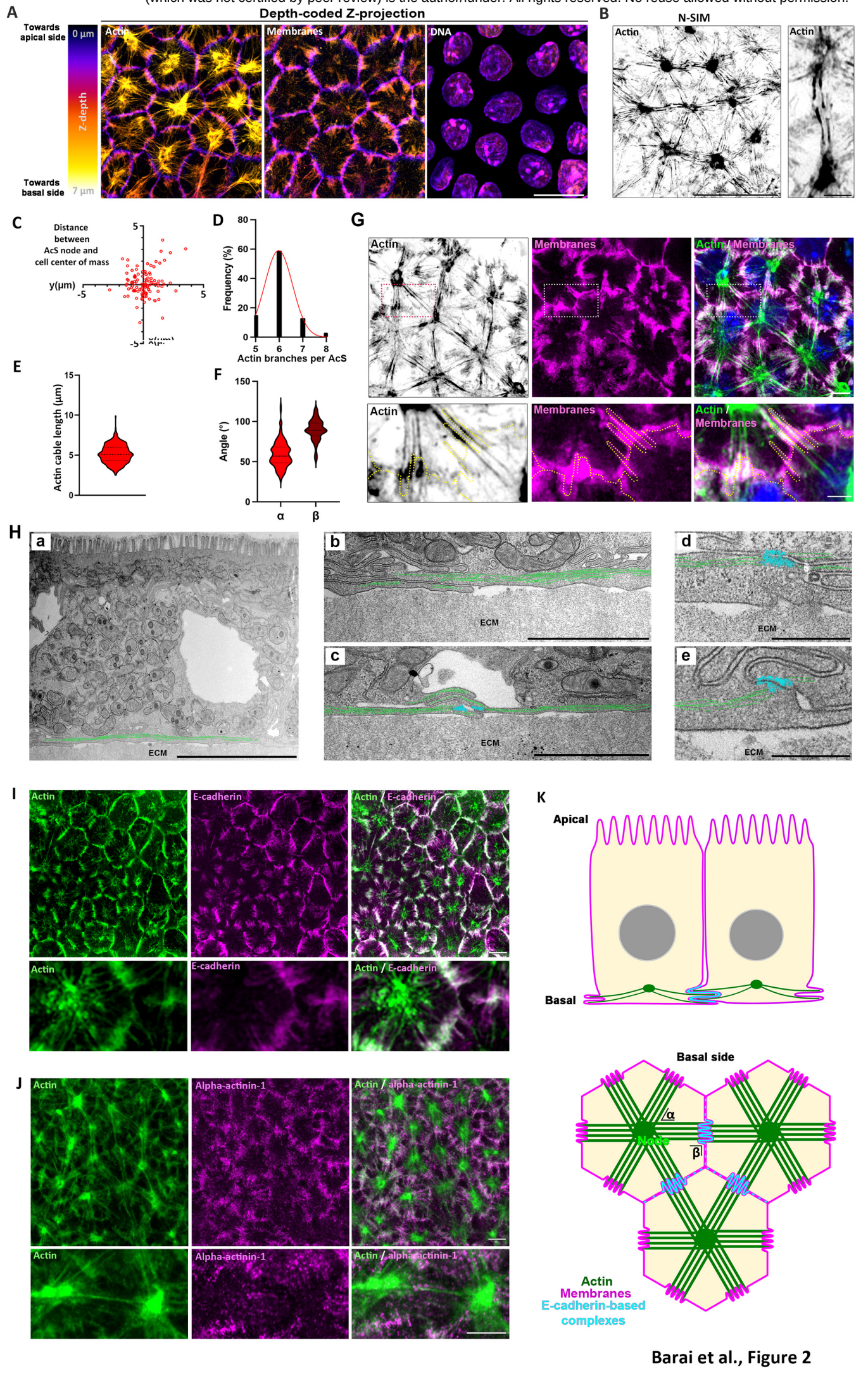

Barai et al., Figure 2

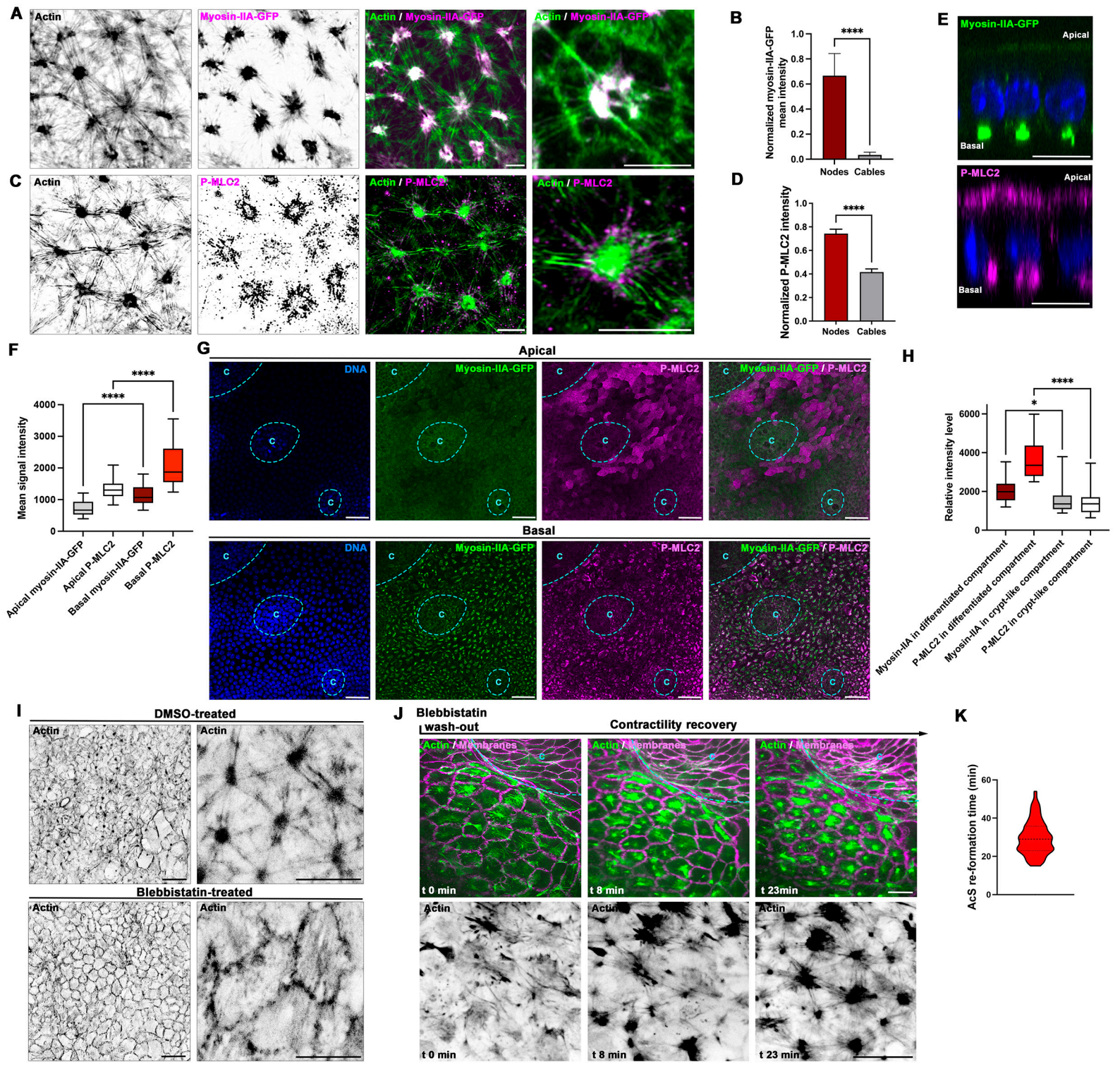

Barai et al., Figure 3

Organoid-derived monolayers

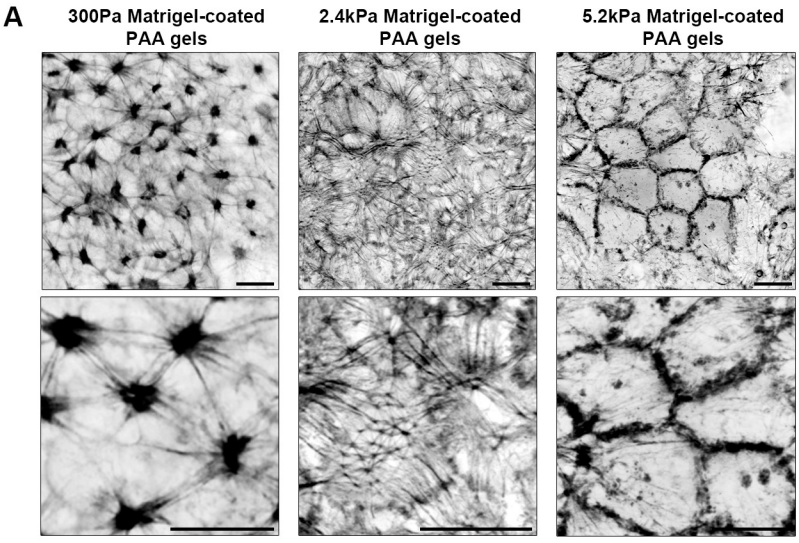

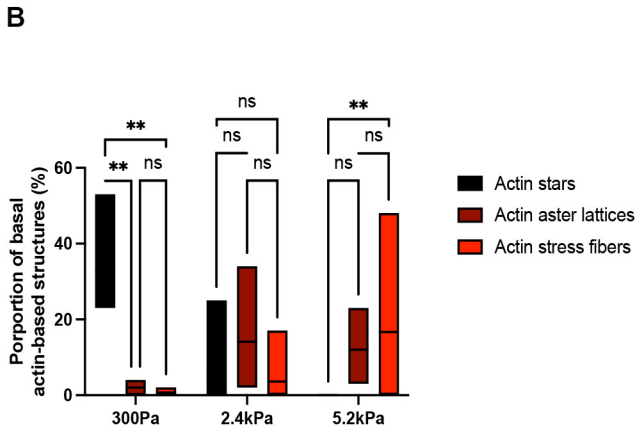

Caco-2 cells

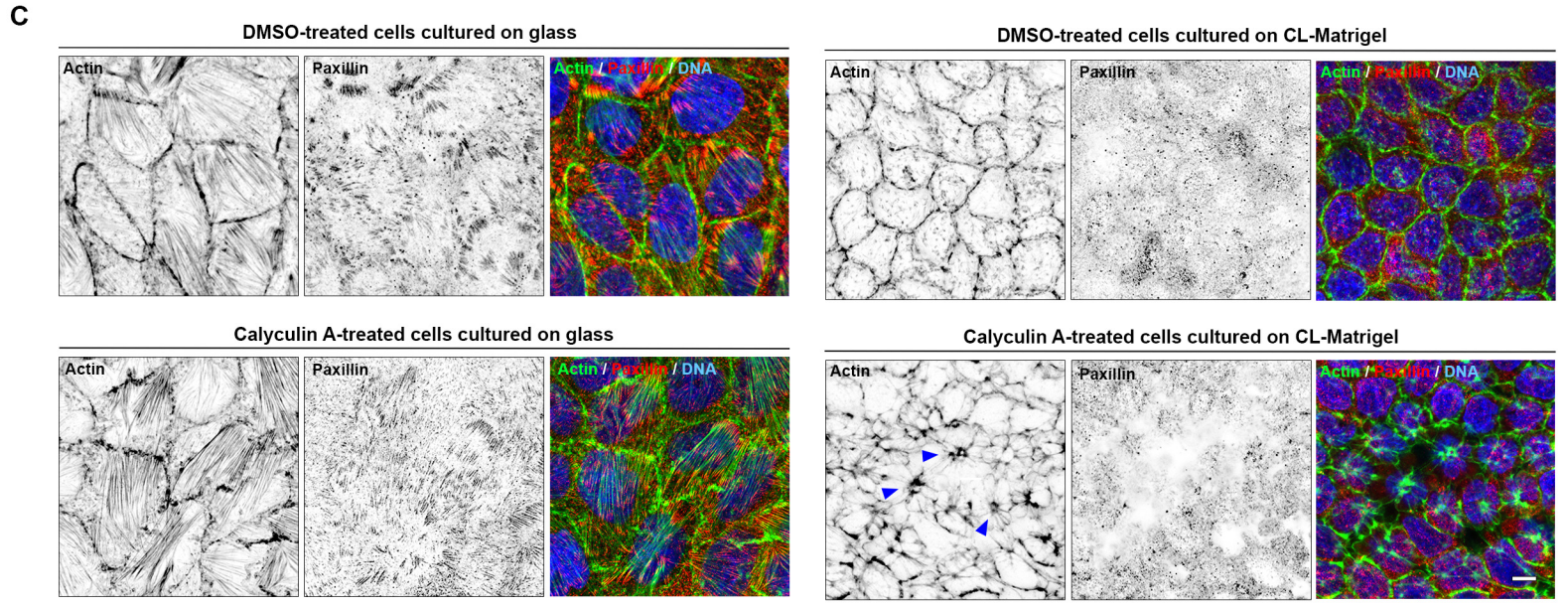

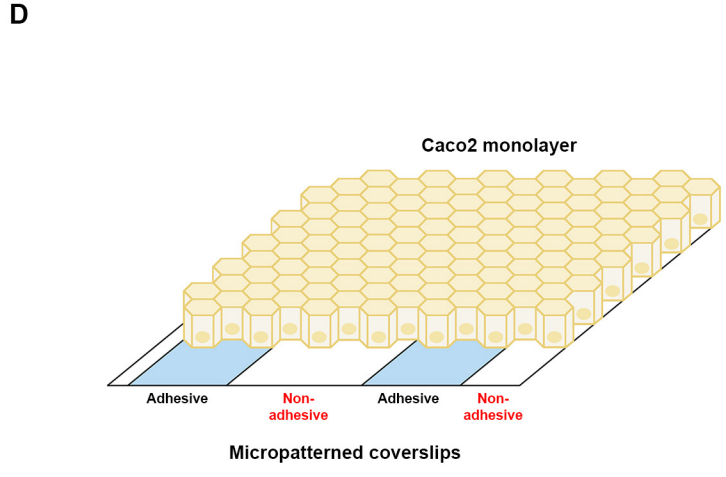

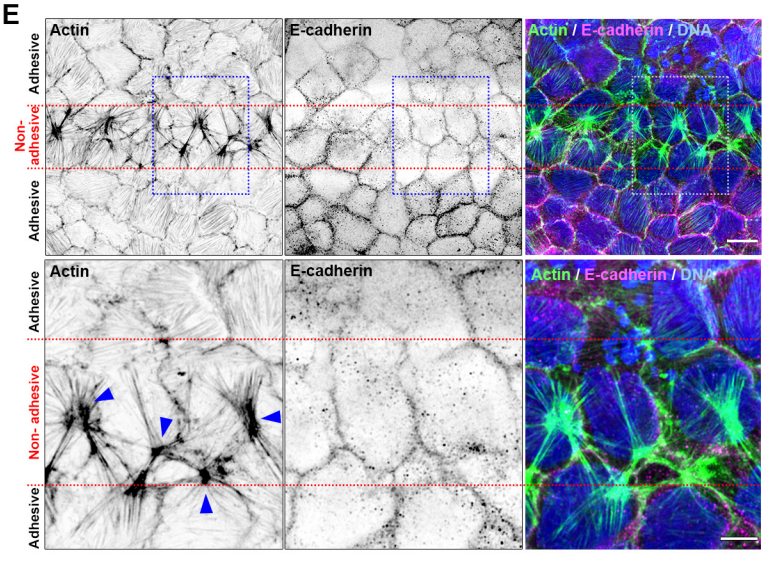

Barai et al., Figure 4

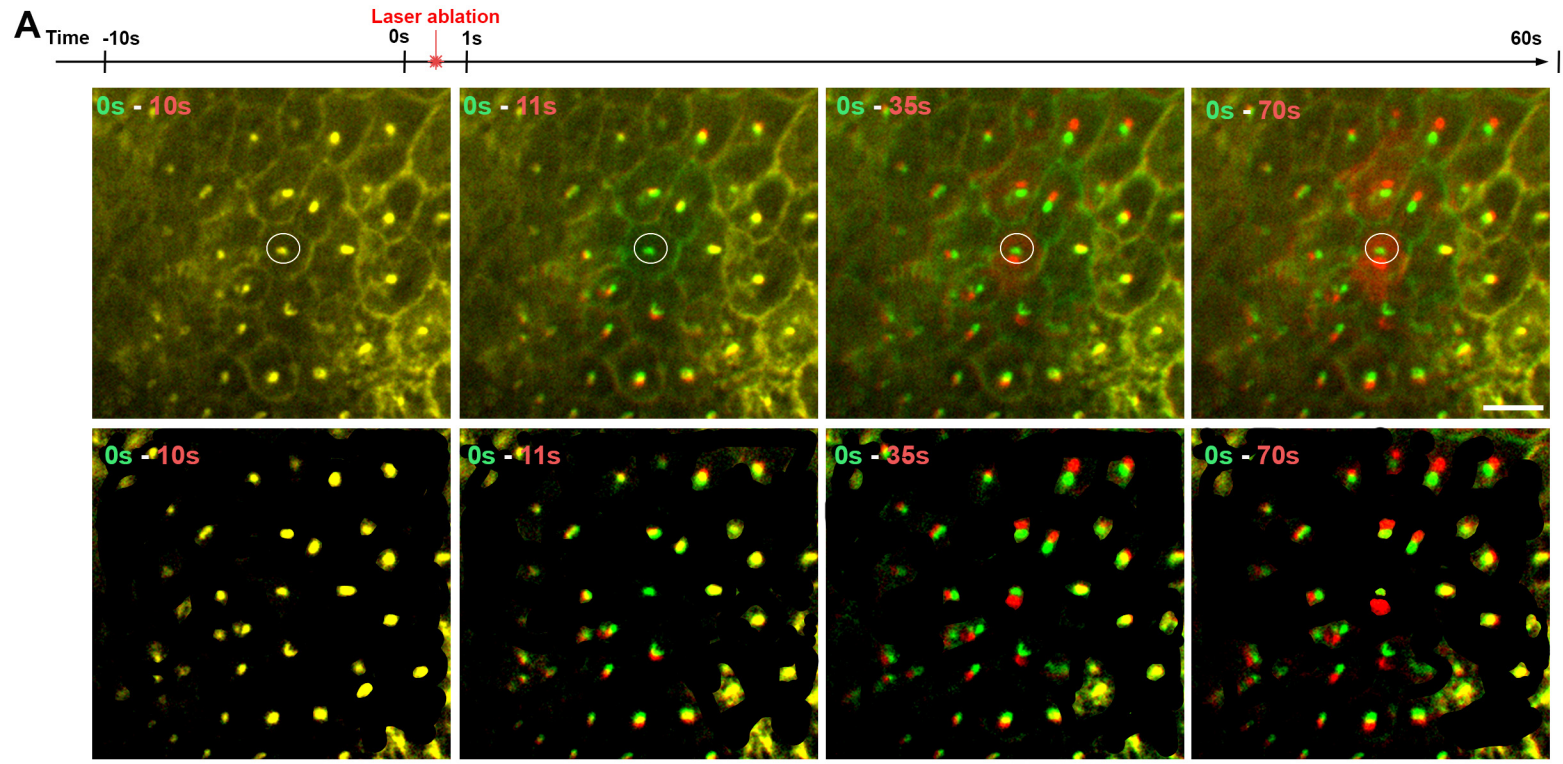

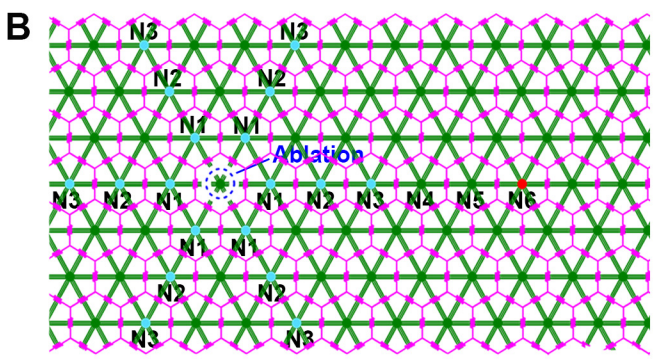

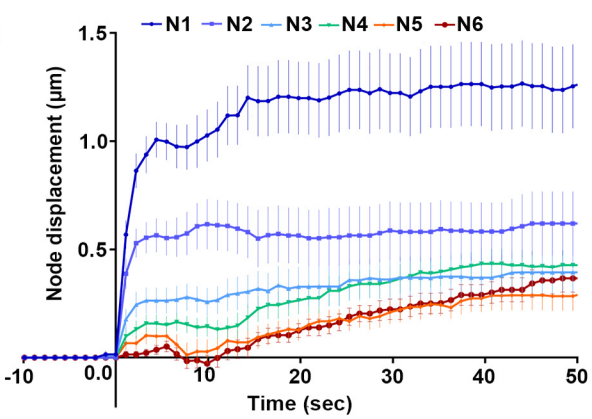

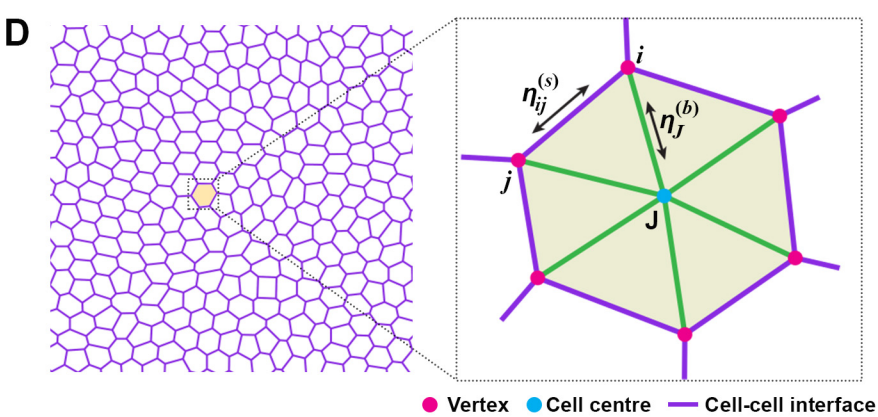

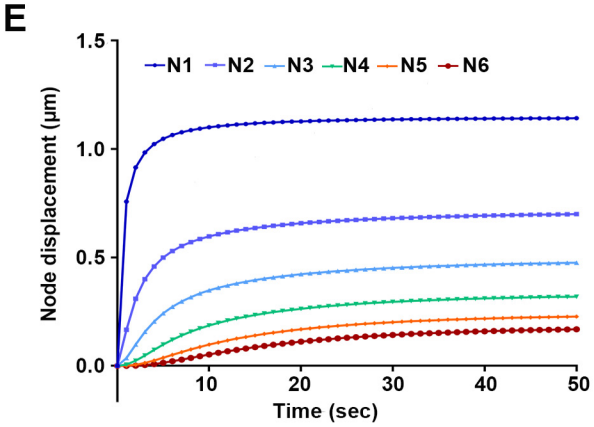

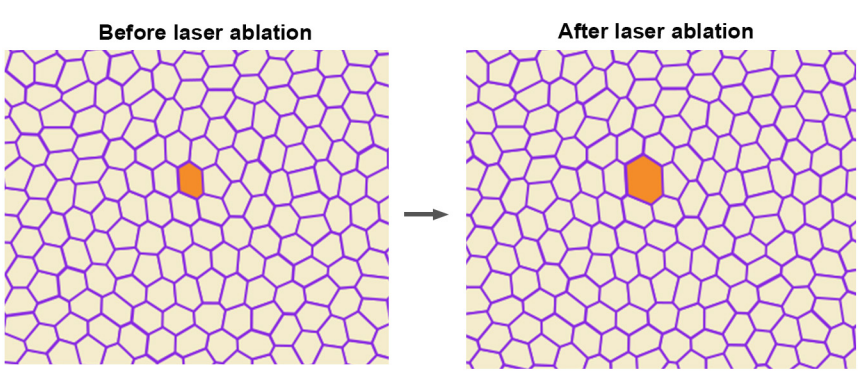

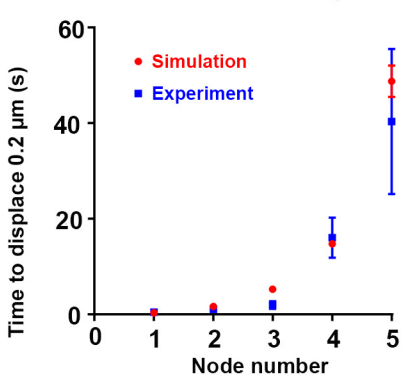

Barai et al. Figure 6

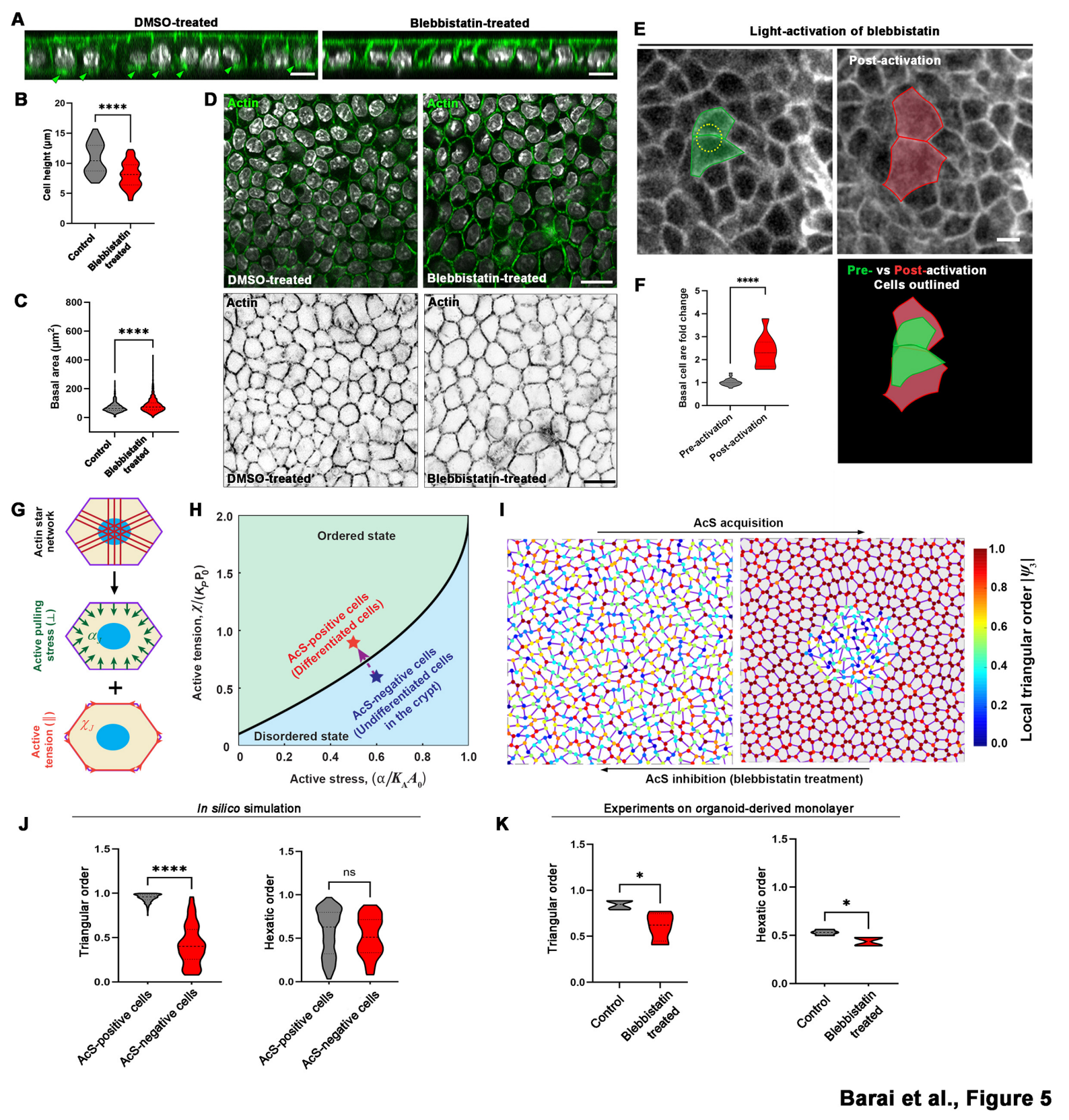

Barai et al., Figure 5

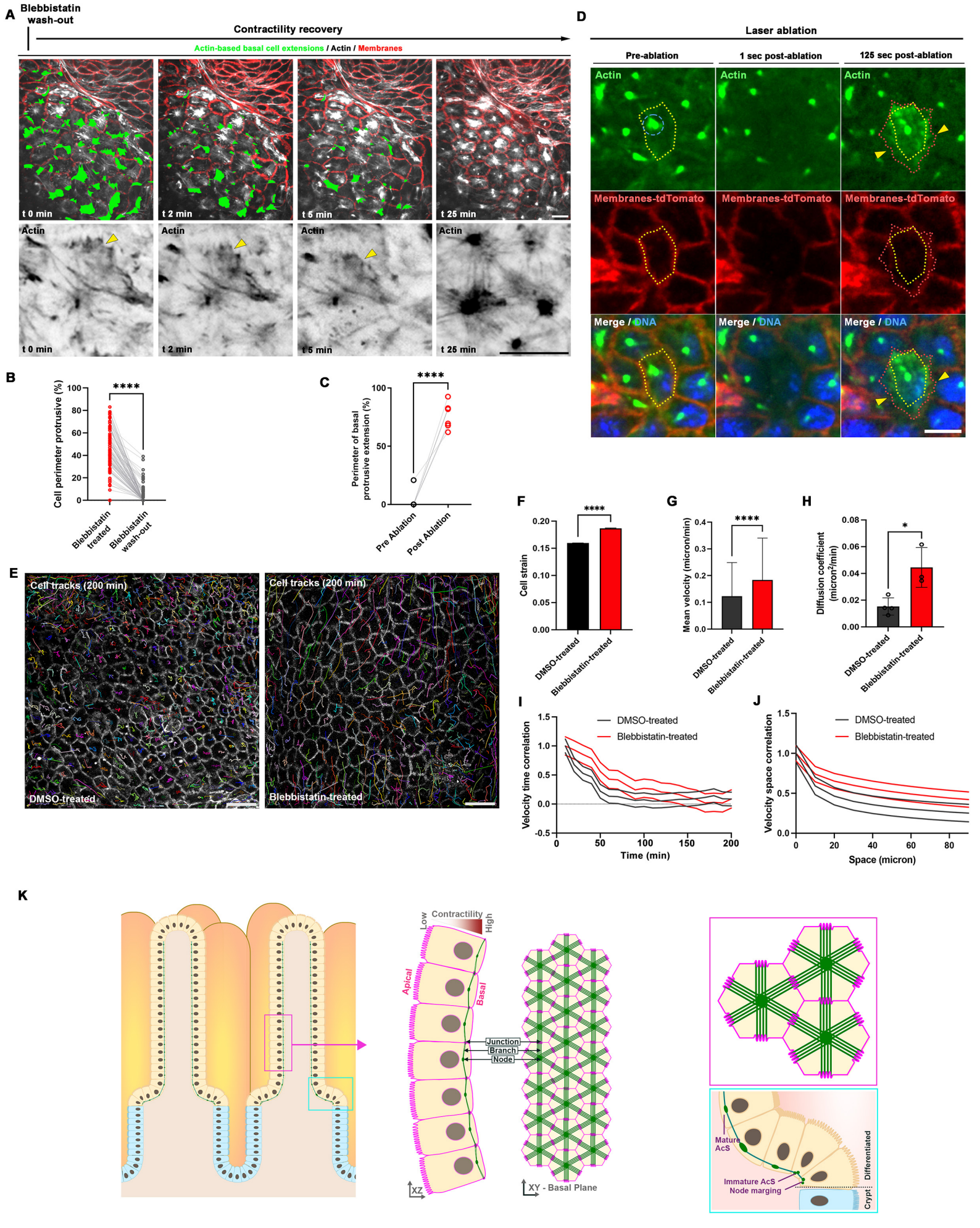

Barai et al., Figure 7

Barai et al.

SUPPLEMENTARY INFORMATION FILE

Supplementary Figures S1- S4

Supplementary Information: File detailing the vertex model simulation procedure are in the online version of the paper.

SUPPLEMENTARY FIGURES

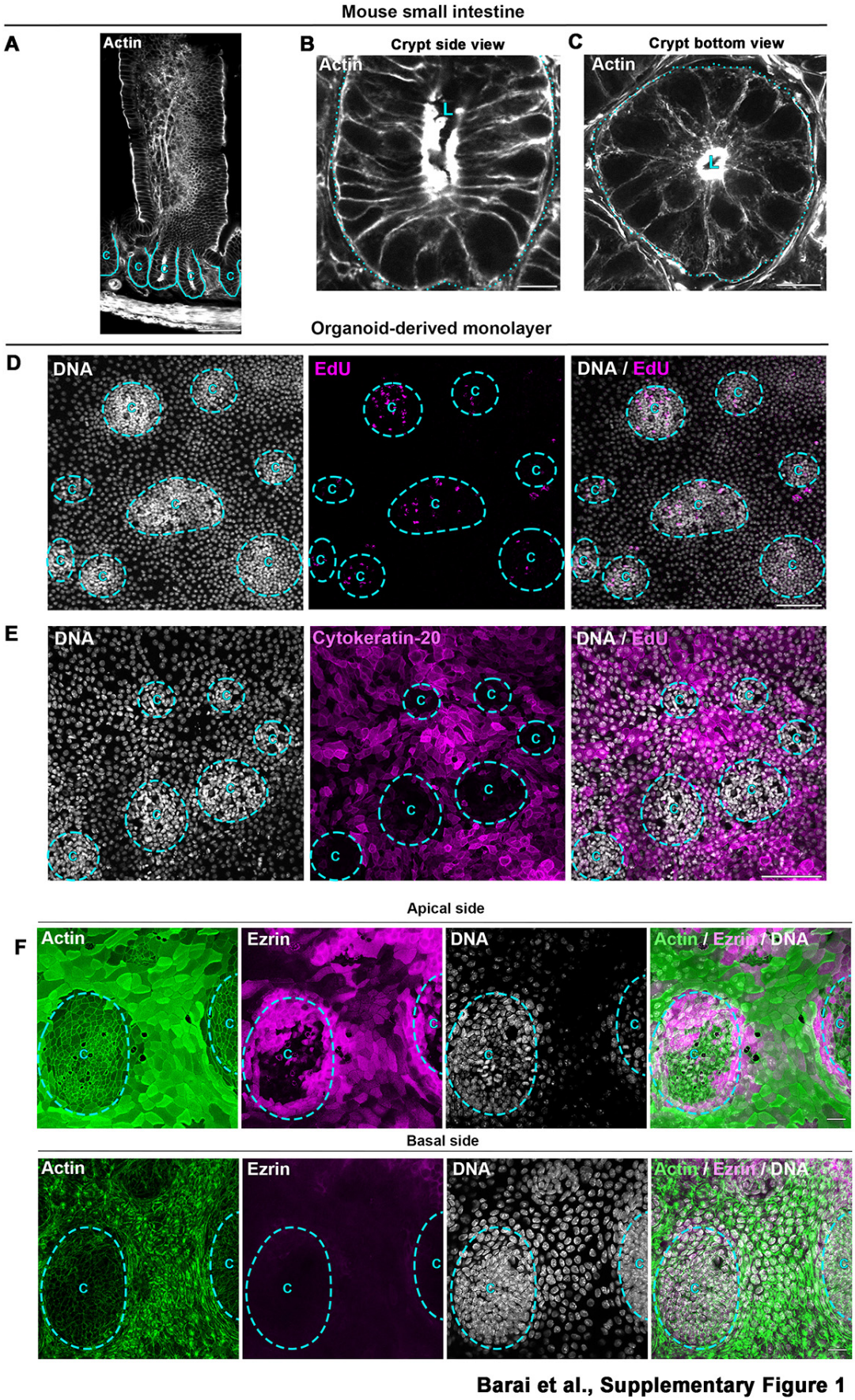

Barai et al., Supplementary Figure 1

Supplementary Figure 1: (A-C) Confocal analysis of actin distribution in the mouse crypt compartment. Crypt side view (B) and bottom view (C) are shown. Crypt domains are delimited with blue line. L, crypt lumen. Scale bar A 100 µm, B-C 10 µm. **(D-E)** Confocal analysis of EdU (D) and cytokeratin-20 (E) distribution in organoid-derived monolayers. Nuclei are sown in gray. Crypt-like domains are delimited in blue. C, crypt-like domain. Scale bar (D), 20 µm, (E) 30µm. Scale bar, 100 µm. **(F)** Confocal analysis of actin (green), ezrin (magenta) and DNA (gray) in the apical or basal side of organoid-derived monolayers. Crypt-like domains are delimited in blue. C, crypt-like domain. Scale bar, 20 µm.

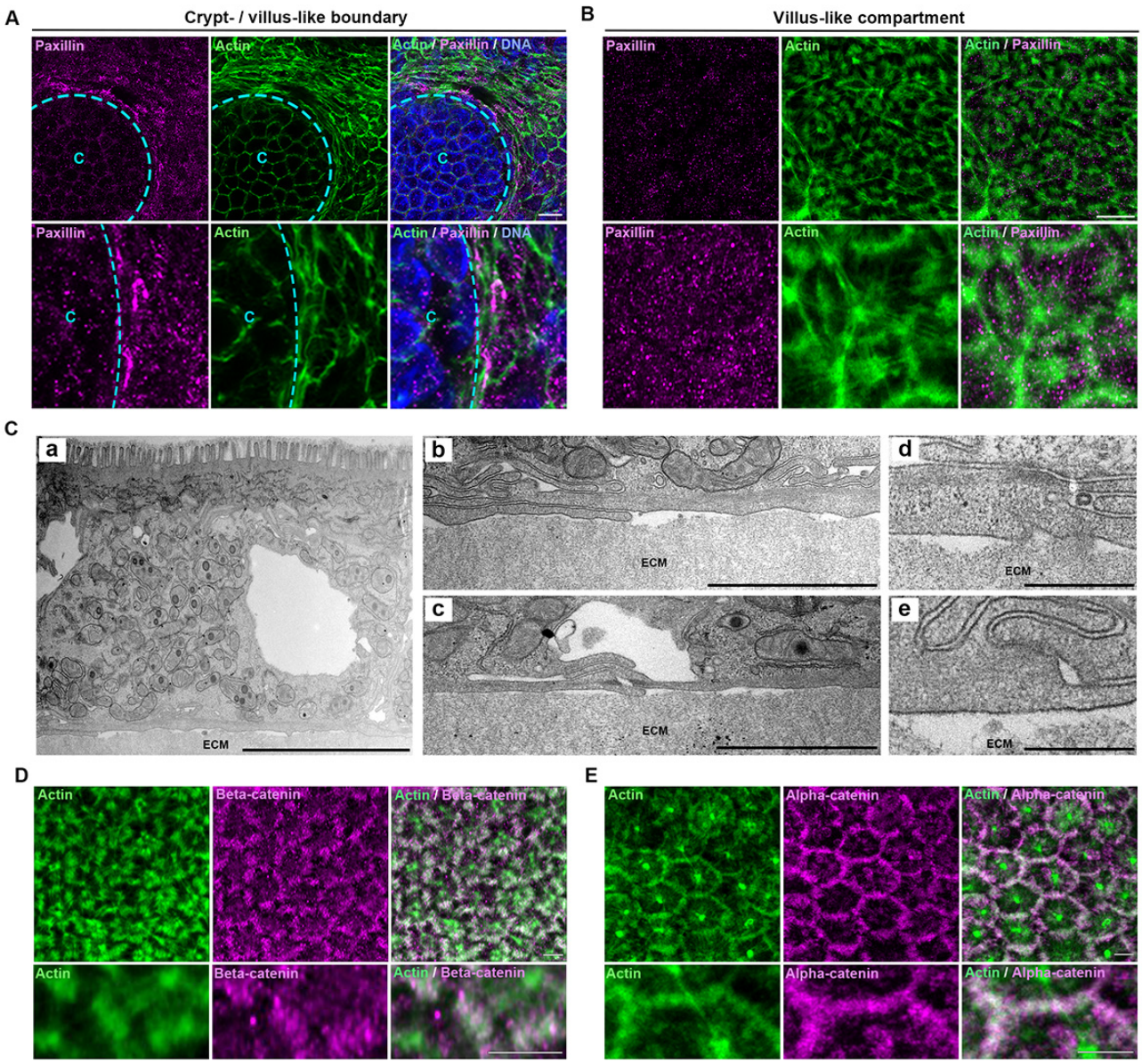

Supplementary Figure 2: (A-B) Airy scan confocal analysis of paxillin (magenta) and actin (green) in the area of crypt- / villus-like boundary or in the differentiated compartment. Crypt-like domains are delimited in blue. C, crypt-like domain. Scale bar, 10 µm. **(Ca-e)** Transmission electron microscopy analysis of the basal domain of differentiated cells in organoid-derived monolayers. ECM, extracellular matrix. Scale bars, (a) 5 µm, (b-c) 2 µm, (d-e) 0.5µm. **(D-E)** Confocal analysis of β-catenin (magenta) or α-catenin (magenta) and actin (green) in the differentiated compartment of organoid-derived monolayers. Scale bar, 5µm.

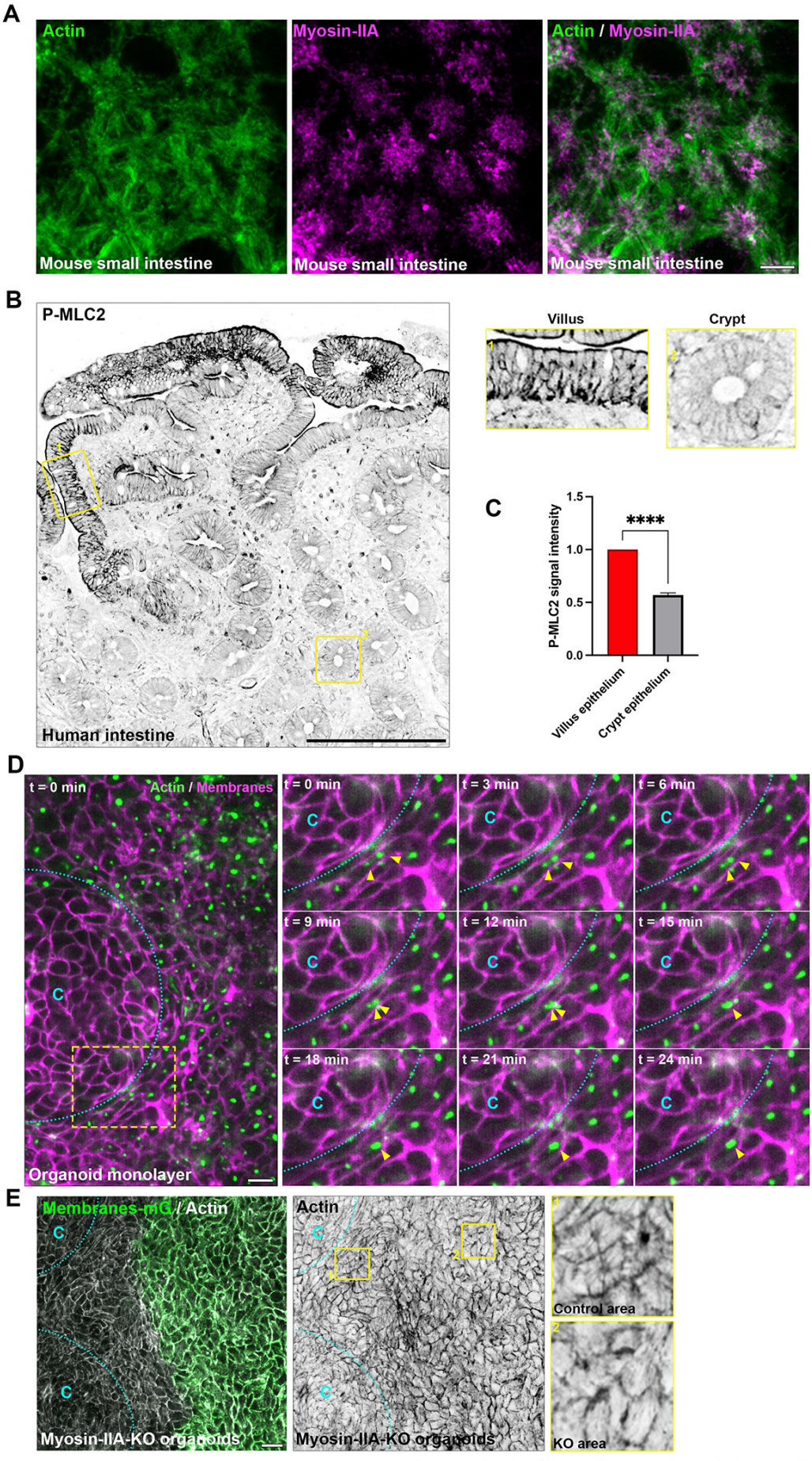

Barai et al., Supplementary Figure 3

Supplementary Figure 3: (A) Confocal analysis of actin (green) and myosin-IIA (magenta) in the basal domain of differentiated cells along the villus of the mouse small intestine. Scale bar, 5 µm. **(B)** Confocal analysis of P-MLC2 distribution in the human intestinal tissue. Areas boxed in yellow are presented on the right. Scale bar, 200 µm. **(C)** Statistical analyses of the signal intensity of P-MLC2 in the villus epithelium and the crypt epithelium in the human small intestine. Mean normalized signal intensity in the villus epithelium = 1, in the crypt epithelium = 0.5691±0.021. N (intestinal biopsies) = 3. Unpaired t-test, ****p<0.0001. **(D)** Time-lapse analysis of AcS formation at exit of the crypt-like domain in organoid-derived monolayers. Actin (green) and membranes (red) are shown. Yellow arrowheads point toward one AcS formation. Crypt-like domains are delimited in blue. C, crypt. Scale bar, 10 µm. **(E)** Confocal analysis of actin distribution in mosaic myosin-IIA-KO organoid-derived monolayers. Myosin-IIA-KO-induced cells are positive for membranes-mG (green). Crypt-like domains are delimited in blue. C, crypt. Areas boxed in yellow are presented on the right. Scale bar, 20 µm.

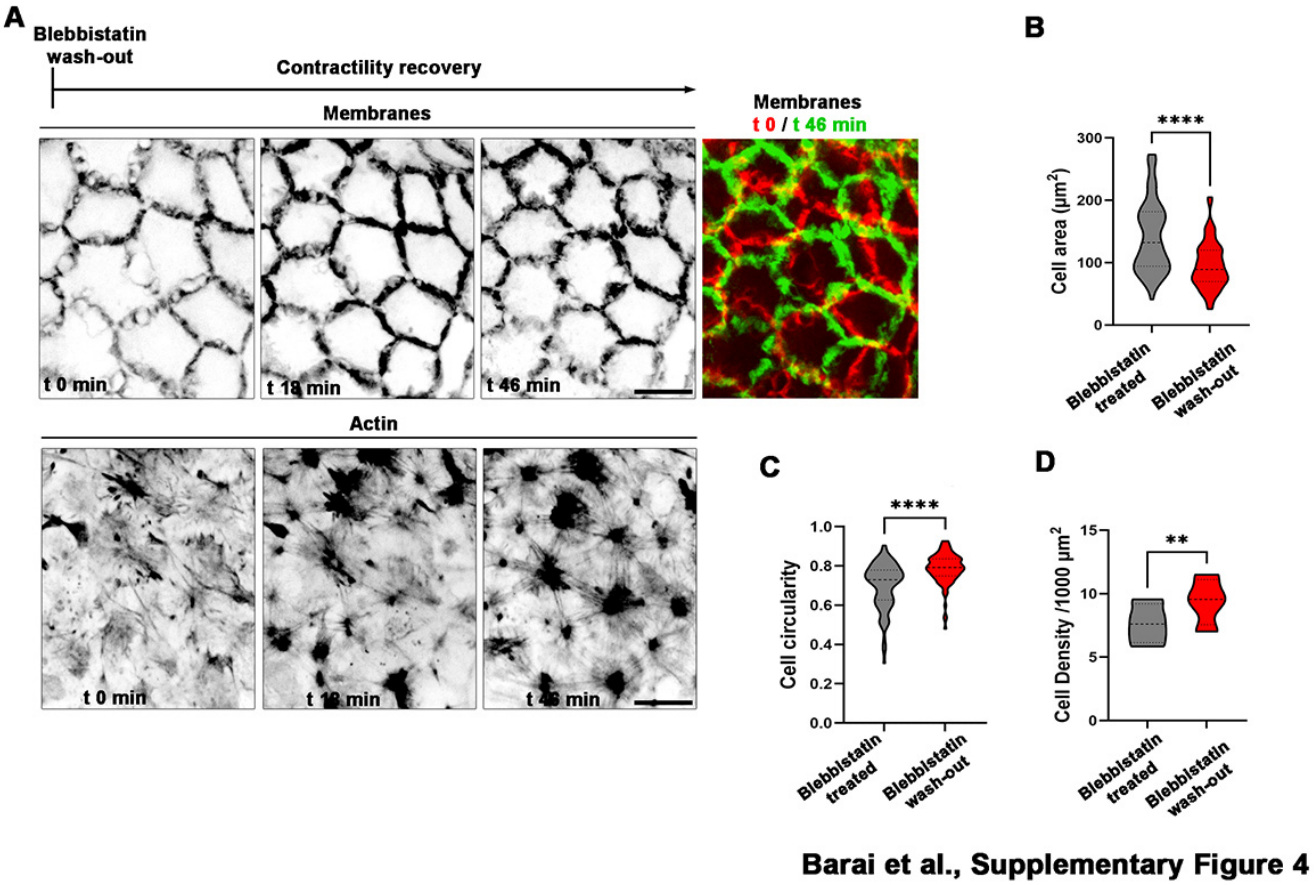

Supplementary Figure 4: (A) Time-lapse of CellMaskActin and membranes-tdTomato organoid-derived monolayer after 1h blebbistatin treatment and then wash-out (t = 0min). Color-coded t-projection of time-lapse series of membranes-tdTomato signal at the basal domain during contractility recovery in organoid-derived monolayer is shown (t=0min in green, t = 46 min in red). Scale bar, 10 µm. **(B)** Statistical analysis of basal cell area before and after blebbistatin wash-out. Mean basal area before = 141.75±5.67 (mean±S.E.M), after = 95.67±3.69. N = 4 experiments, n = 100 cells. Paired t-test, ****p<0.0001. **(C)** Statistical analysis of basal cell circularity before and after blebbistatin wash-out. Mean basal circularity before = 0.70±0.01 (mean±S.E.M), after = 0.79±0.01. n = 100 cells. Paired t-test, ****p<0.0001. **(D)** Statistical analysis of cell density before and after blebbistatin wash-out. Mean cell density before = 7.65±0.79 (mean±S.E.M), after = 9.40±0.93. Paired t-test, **p=0.004.

Supplementary Information

A multicellular actin star network underpins epithelial organization and connectivity

Barai et al.

In these notes, we present additional details about our numerical vertex model implementation.

Contents

I. MODEL 1: ACS FORMATION MODELLED THROUGH A MODULATION OF THE BULK ACTIVE STRESS

A. Computational model

Dynamical equation We consider a vertex model implementation [1–3], with the following dynamics for each vertex,

$$\underbrace{\boldsymbol{F}_i^{(\mathrm{friction})}}_{\text{Friction}} + \underbrace{\boldsymbol{F}_i^{(\mathrm{viscous})}}_{\text{Cell viscosity}} + \underbrace{\boldsymbol{F}_i^{(\mathrm{elastic})}}_{\text{Cell elasticity}} + \underbrace{\boldsymbol{F}_i^{(\mathrm{active})}}_{\text{Actin star network contractility}} = \boldsymbol{0}, \tag{S1}$$

where we consider:

1. $\boldsymbol{F}_i^{(\mathrm{friction})} = -\xi \boldsymbol{v}_i$ is the friction force between the monolayer and the substrate, ξ being called the friction coefficient and $\boldsymbol{v}_i = \mathrm{d}\boldsymbol{r}_i/\mathrm{d}t$ being the velocity of the vertex i.

2. $\boldsymbol{F}_i^{(\mathrm{viscous})}$ encompasses both dissipation at the cell–cell interfaces (viscous modulus $\eta_{ij}^{(\mathrm{s})}$) and within the cell bulk (viscous modulus $\eta_J^{(\mathrm{b})}$). We consider:

$$\boldsymbol{F}_i^{(\mathrm{viscous})} = \sum_{j\in V_i} (\eta_{ij}^{(\mathrm{s})} \boldsymbol{t}_{i,j} \cdot (\boldsymbol{v}_j - \boldsymbol{v}_i)) \boldsymbol{t}_{i,j} + \sum_{J\in C_i} (\eta_J^{(\mathrm{b})} \boldsymbol{t}_{i,J} \cdot (\boldsymbol{v}_J - \boldsymbol{v}_i)) \boldsymbol{t}_{i,J}, \tag{S2}$$

where $\boldsymbol{t}_{i,\alpha} = (\boldsymbol{r}_\alpha - \boldsymbol{r}_i)/|\boldsymbol{r}_i - \boldsymbol{r}_\alpha|$ is a unit vector from the vertex i to, either a neighbouring vertex ($\alpha = j$), or to the cell geometric centre ($\alpha = J$) with coordinates

$$\boldsymbol{r}_J = \frac{1}{n_J} \sum_{j\in cell} \boldsymbol{r}_j, \tag{S3}$$

where n_J the number of vertices of J-th cell. We refer to ref. [4] for more details on the numerical implementation. In this study, we focus on the case of a uniform viscosity $\eta_{ij}^{(\mathrm{s})} = \eta_J^{(\mathrm{b})} = \eta$.

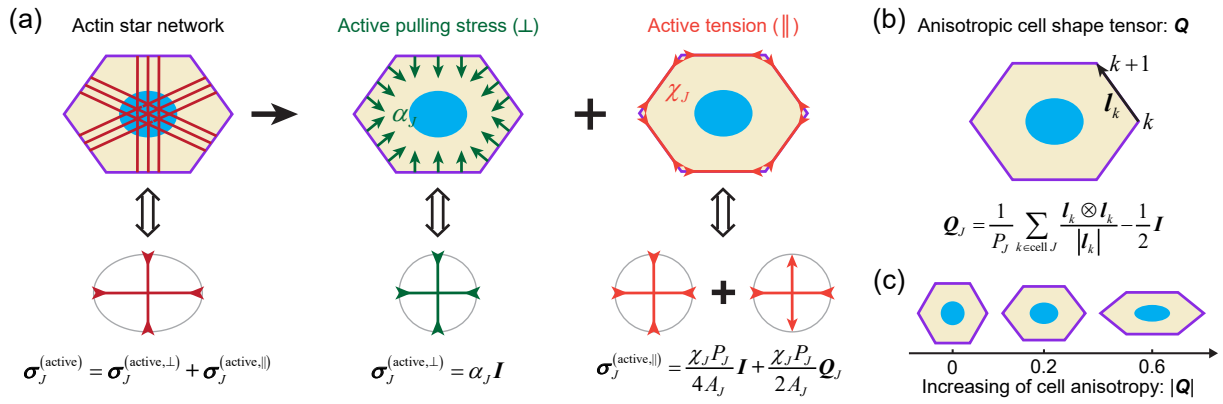

Figure S1: Mechanical characterization of the contractility of the actin star network with a cell by an active pulling stress and an active tension. (a) Mechanical description of the actin star network contractility within a cell by active stresses, $\boldsymbol{\sigma}^{(\text{active})} = \boldsymbol{\sigma}^{(\text{active},\perp)} + \boldsymbol{\sigma}^{(\text{active},\parallel)}$ with $\boldsymbol{\sigma}^{(\text{active},\perp)} = \alpha_J \boldsymbol{I}$ quantifying the pulling force normal to cell edges and $\boldsymbol{\sigma}^{(\text{active},\parallel)} = \chi_J P_J/(4A_J)\boldsymbol{I} + \chi_J P_J/(2A_J)\boldsymbol{Q}_J$ quantifying an active tension parallel to cell edges. (b) Sketch of the anisotropic cell shape tensor $\boldsymbol{Q}$. (c) Examples of cell shapes as a function of the magnitude of the cell anisotropic tensor $|\boldsymbol{Q}|$.

3. $\boldsymbol{F}_i^{(\text{elastic})}$ is the elastic force stemming from the variation of the cell shape, which can be expressed by, $\boldsymbol{F}_i^{(\text{elastic})} = -\partial E/\partial \boldsymbol{r}_i$ with the mechanical energy [2, 5–8]:

$$E = \underbrace{\sum_{J=1}^{N} \frac{1}{2} K_A (A_J - A_0)^2}_{\text{Cell area elasticity}} + \underbrace{\sum_{J=1}^{N} \frac{1}{2} K_P (P_J - P_0)^2}_{\text{Cell perimeter elasticity}}, \tag{S4}$$

where K_A and K_P are the rigidities associated with cell area and cell perimeter; A_0 and P_0 are the preferred cell area and the preferred cell perimeter, respectively; A_J and P_J are the actual area and perimeter of the J-th cell, respectively.

4. the active force $\boldsymbol{F}_i^{(\text{active})}$ corresponds to the contribution of the multicellular actin; we decompose the actin star network into two contributions, resulting from:

   - (4.1) an active pulling stress $\boldsymbol{\sigma}_J^{(\text{active},\perp)} = \alpha_J \boldsymbol{I}$ with $\alpha_J \geq 0$ quantifies the intensity of the active pulling stress induced by the contractility of the actin star network within the J-th cell, which describes the active pulling force normal to cell edges, see Fig. S1(a);
   - (4.2) an active tension $\chi_J > 0$ parallel to edges of the J-th cell, see Fig. S1(a), which results in the following $\boldsymbol{F}_k^{(\text{AT})}$ force applied on the k-th vertex of the J-th cell:

$$\boldsymbol{F}_k^{(\text{AT})} = \frac{1}{2}\chi_J \frac{\boldsymbol{l}_k}{|\boldsymbol{l}_k|} - \frac{1}{2}\chi_J \frac{\boldsymbol{l}_{k-1}}{|\boldsymbol{l}_{k-1}|}, \tag{S5}$$

   where $\boldsymbol{l}_k = \boldsymbol{r}_{k+1} - \boldsymbol{r}_k$ the k-th edge vector of the J-th cell.

B. Theoretical analysis: active-stress driven liquid-to-solid phase transition

In this section, we show that the active pulling stress α_J is equivalent to renormalizing the preferred area of the J-th cell as: $A_{0,J} = A_0 - \alpha_J/K_A$; and that the active tension χ_J is equivalent to renormalizing the preferred perimeter of the J-th cell as: $P_{0,J} = P_0 - \chi_J/(2K_P)$. Our derivation is based on the analytical derivation of the total stresses within cells.

We express the active stress induced by the actin star network by (Fig. S1(a)):

$$\boldsymbol{\sigma}_J^{(\text{active})} = \boldsymbol{\sigma}_J^{(\text{active},\perp)} + \boldsymbol{\sigma}_J^{(\text{active},\parallel)}, \tag{S6}$$

where

$$\boldsymbol{\sigma}_J^{(\text{active},\perp)} = \alpha_J \boldsymbol{I}, \tag{S7}$$

quantifies the active stress induced by the active pulling stress (i.e., pulling forces normal to the cell edges, Fig. S1(a)), and, using the Batchelor formula [8–11],

$$\boldsymbol{\sigma}_J^{(\text{active},\parallel)} = -\frac{1}{A_J} \sum_{k\in\text{cell}\ J} \boldsymbol{r}_k \otimes \boldsymbol{F}_k^{(\text{AT})}, \tag{S8}$$

quantifies the active stress induced by the active tension parallel to cell edges (Fig. S1(a)). Substituting Eq. (S5) into Eq. (S8), we obtain

$$\begin{aligned}
\boldsymbol{\sigma}_J^{(\text{active},\parallel)} &= -\frac{1}{A_J} \sum_{k\in\text{cell}\ J} \boldsymbol{r}_k \otimes \left(\frac{1}{2}\chi_J \frac{\boldsymbol{l}_k}{|\boldsymbol{l}_k|} - \frac{1}{2}\chi_J \frac{\boldsymbol{l}_{k-1}}{|\boldsymbol{l}_{k-1}|} \right) = -\frac{\chi_J}{2A_J} \sum_{k\in\text{cell}\ J} \boldsymbol{r}_k \otimes \left(\frac{\boldsymbol{l}_k}{|\boldsymbol{l}_k|} - \frac{\boldsymbol{l}_{k-1}}{|\boldsymbol{l}_{k-1}|} \right) \\
&= -\frac{\chi_J}{2A_J} \sum_{k\in\text{cell}\ J} \left(\boldsymbol{r}_k \otimes \frac{\boldsymbol{l}_k}{|\boldsymbol{l}_k|} - \boldsymbol{r}_k \otimes \frac{\boldsymbol{l}_{k-1}}{|\boldsymbol{l}_{k-1}|} \right) = -\frac{\chi_J}{2A_J} \sum_{k\in\text{cell}\ J} \left(\boldsymbol{r}_k \otimes \frac{\boldsymbol{l}_k}{|\boldsymbol{l}_k|} - \boldsymbol{r}_{k+1} \otimes \frac{\boldsymbol{l}_k}{|\boldsymbol{l}_k|} \right) \\
&= \frac{\chi_J}{2A_J} \sum_{k\in\text{cell}\ J} \frac{\boldsymbol{l}_k \otimes \boldsymbol{l}_k}{|\boldsymbol{l}_k|} = \frac{\chi_J P_J}{2A_J} \left(\boldsymbol{Q}_J + \frac{1}{2}\boldsymbol{I} \right) = \frac{\chi_J P_J}{4A_J} \boldsymbol{I} + \frac{\chi_J P_J}{2A_J} \boldsymbol{Q}_J,
\end{aligned} \tag{S9}$$

where $\boldsymbol{Q}_J$ is a traceless anisotropic cell shape tensor (Fig. S1(b)), defined as [8, 12]

$$\boldsymbol{Q}_J = \frac{1}{P_J} \sum_{k\in\text{cell}\ J} \frac{\boldsymbol{\ell}_k \otimes \boldsymbol{\ell}_k}{|\boldsymbol{\ell}_k|} - \frac{1}{2}\boldsymbol{I}. \tag{S10}$$

For isotropic cell shape, e.g., regular hexagonal shape, $\boldsymbol{Q}_J = \boldsymbol{0}$; the magnitude $|\boldsymbol{Q}_J|$ quantifies cell anisotropy (Fig. S1(c)). Overall, the active stress induced by the actin star network can be expressed as:

$$\boldsymbol{\sigma}_J^{(\text{active})} = \boldsymbol{\sigma}_J^{(\text{active},\perp)} + \boldsymbol{\sigma}_J^{(\text{active},\parallel)} = \left(\alpha_J + \frac{\chi_J P_J}{4A_J} \right) \boldsymbol{I} + \frac{\chi_J P_J}{2A_J} \boldsymbol{Q}_J. \tag{S11}$$

We recall that the elastic stress corresponding to the mechanical energy Eq. (S4) reads [8, 13]:

$$\boldsymbol{\sigma}_J^{(\text{elastic})} = \left[K_A \left(A_J - A_0 \right) + \frac{1}{2} \frac{K_P P_J \left(P_J - P_0 \right)}{A_J} \right] \boldsymbol{I} + \frac{K_P P_J \left(P_J - P_0 \right)}{A_J} \boldsymbol{Q}_J. \tag{S12}$$

Therefore, the total stress within the J-th cell reads:

$$\begin{aligned}
\boldsymbol{\sigma}_J &= \boldsymbol{\sigma}_J^{(\text{elastic})} + \boldsymbol{\sigma}_J^{(\text{active})} \\
&= \left[K_A \left(A_J - A_0 \right) + \alpha_J + \frac{1}{2} \frac{K_P P_J \left(P_J - P_0 \right)}{A_J} + \frac{1}{4} \frac{\chi_J P_J}{A_J} \right] \boldsymbol{I} + \left[\frac{K_P P_J \left(P_J - P_0 \right)}{A_J} + \frac{1}{2} \frac{\chi_J P_J}{A_J} \right] \boldsymbol{Q}_J \\
&= \left[K_A \left(A_J - A_{0,J} \right) + \frac{1}{2} \frac{K_P P_J \left(P_J - P_{0,J} \right)}{A_J} \right] \boldsymbol{I} + \frac{K_P P_J \left(P_J - P_{0,J} \right)}{A_J} \boldsymbol{Q}_J,
\end{aligned} \tag{S13}$$

where

$$A_{0,J} = A_0 - \frac{\alpha_J}{K_A}, \tag{S14}$$

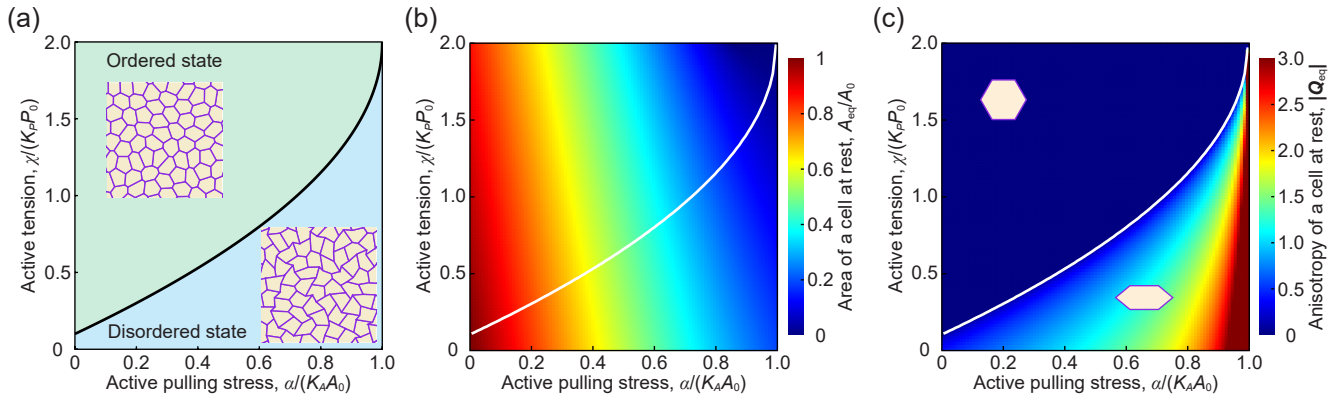

Figure S2: Theoretical analysis of cell area and cell anisotropy dictated by the active pulling stress α and the active tension χ. (a) Critical rigidity transition line Eq. (S19) (solid black line) and typical morphology of a cell monolayer within each phase. (b) The area of a hexagonal cell at rest (white line: rigidity transition line Eq. (S19)) (c) Theoretical prediction [8] of the anisotropy $|\boldsymbol{Q}|$ of a single cell at rest. (white line: rigidity transition line Eq. (S19)). Parameters: $K_A = 1$, $A_0 = 1$, $K_P = 0.02$, and $P_0 = 4$.

is a rescaled preferred area of the J-th cell, modulated by the isotropic active stress level α_J, and

$$P_{0,J} = P_0 - \frac{\chi_J}{2K_P}, \tag{S15}$$

is a rescaled preferred perimeter of the J-th cell, modulated by the active tension level χ_J.

Effective mechanical energy formalism. The total stress Eq. (S13) corresponds to an effective mechanical energy of the J-th cell,

$$E_J^{(\mathrm{eff})} = \frac{1}{2}K_A(A_J - A_{0,J})^2 + \frac{1}{2}K_P(P_J - P_{0,J})^2, \tag{S16}$$

which satisfies

$$\boldsymbol{\sigma}_J = -\frac{1}{A_J}\sum_{k\in\mathrm{cell}\ J} \boldsymbol{r}_k \otimes \left(-\frac{\partial E_J^{(\mathrm{eff})}}{\partial \boldsymbol{r}_k}\right). \tag{S17}$$

Therefore, the contractility of the actin star network can be mimicked by a renormalized mechanical energy, $E_J^{(\mathrm{eff})}$.

Cellular target shape index modulated by the actin star network. Equations (S14) and (S15) show that the actin star network within cells plays a role in modulating the target shape index of the cell [6],

$$s_{0,J} = \frac{P_{0,J}}{\sqrt{A_{0,J}}} = \frac{P_0}{\sqrt{A_0}}\frac{1 - \dfrac{\chi_J}{2K_P P_0}}{\sqrt{1 - \dfrac{\alpha_J}{K_A A_0}}}. \tag{S18}$$

An increase in the active pulling stress α_J leads to an increase in the target shape index $s_{0,J}$, making cells more elongated; while an increase in the active tension χ_J leads to a decrease in the target shape index $s_{0,J}$, making cells more rounded.

Following [6], letting $s_{0,J} = s_0^\star$ leads to a critical line of rigidity transition in the $(\alpha_J\ ,\ \chi_J)$ space:

$$\chi_J^\star = 2K_P P_0\left(1 - s_0^\star\frac{\sqrt{A_0}}{P_0}\sqrt{1 - \frac{\alpha_J}{K_A A_0}}\right), \tag{S19}$$

where $s_0^\star$ is a critical target shape index beyond which the cell monolayer behaves as a disordered liquid; $s_0^\star \approx 3.81$ for disordered cellular system [6]. When the active tension is strong enough, i.e., $\chi_J > \chi_J^\star$, the cell monolayer behaves as a liquid, exhibiting a disordered and elongated cell shape pattern, see Fig. S2.

C. Numerical simulations

We perform numerical simulations to explore the roles of the multicellular actin star network in the context of

1. the laser ablation of an actin star node,
2. the blebbistatin treatment and wash-out experiment,
3. the progressive cell differentiation.

In all these simulations, we simulated a cell monolayer consisting of $N = 400$ cells in a square box of size $L = \sqrt{NA_0}$, using periodic boundary conditions, see Fig. S4(a). We initialize our simulations from a random Voronoi cell pattern and let the system relax toward an equilibrium state, using the procedure as described in our previous study [8]. We then (i) solve the force balance equation to obtain the motion velocity of each vertex $\{\boldsymbol{v}_i\}$; (ii) move the vertices to new positions using a forward Euler scheme,

$$\boldsymbol{r}_i(t + \Delta t) = \boldsymbol{r}_i + \boldsymbol{v}_i \Delta t, \tag{S20}$$

and (iii) perform T1 topological transitions for all short cell–cell junctions ($l_{ij} < \ell_{\mathrm{T1}} = 0.01\sqrt{A_0}$).

1. *Simulation 1: laser ablation of an actin star node*

Method In such simulations, the activities of all cells are set to be the same before the laser ablation, $\alpha_J = \alpha^{(\mathrm{control})} > 0$ and $\chi_J = \chi^{(\mathrm{control})}$ for $J = 1, 2, 3, \cdots, N$. To model the effect of the laser ablation, we select a cell at the center of the simulation box and set its activity to be zero $\alpha_J = \alpha^{(\mathrm{ablation})} = 0$ and $\chi_J = \chi^{(\mathrm{ablation})} = 0$, see Fig. S4(a). We then let the system relax to a new equilibrium state. We track and measure the displacement of each cell during such a relaxation process. We provide the parameter values in simulations in Table I.

Result We find that the delay in the strain propagation scales with the distance to the ablated cell according to $\tau \sim L^2/K$, i.e. with an effective diffusion of elasticity, denoted K, which is inversely proportional to the friction, i.e. $K \propto 1/\xi$ (see Fig. S4(e)). In the presence of a finite friction, the evolution of the strain is only marginally dependent on the cell-cell viscosity value, see Fig. S4(d). In the limit of vanishing friction ($\xi \to 0$), the strain is propagated at large distances ($N = 8$) in less than a second (blue curve in Fig. S4(e)).

Discussion Diffusion of elasticity is also observed in an optical tweezer mechanical perturbation of cell membranes in the Drosophila embryo [14]. There, the time delay in the strain is measured at $\tau_1 = 150 \pm 85\,\mathrm{ms}$ at a one-cell distance ($\sim 7\mu\mathrm{m}$) to the mechanical perturbation site. Such value lies within the time resolution of our experiments. Based on the diffusion of elasticity scaling, we expect that the corresponding value at the ten-cell distance should scale as $\tau_{10} = 100\tau_1$, corresponding to $\tau_8 \approx 15 \pm 8\,\mathrm{s}$. Such an estimate is compatible with the value at the ten-cell distance measured in one of our experiments, called experiment 1, see Fig. XX; in most other experiments of laser dissection, however, the time delay in the strain remains lower than a few seconds, suggesting a significantly reduced friction as compared to the experiment 1, as depicted in Fig. S4(e)). Overall, the observation that the strain propagation is very rapid is compatible with a very low friction to the substrate.

2. *Simulation 2: blebbistatin treatment (contractility inhibition) and wash-out (contractility recovery)*

Method Here, the activities of all cells are set to be the same before the blebbistatin treatment, $\alpha_J = \alpha^{(\mathrm{control})} > 0$ and $\chi_J = \chi^{(\mathrm{control})} > 0$ for $J = 1, 2, 3, \cdots, N$. To model the effect of the blebbistatin treatment, we select a group of cells with a number $N_{\mathrm{blebbistatin}} = 50$ at the center region of the simulation box and set their activities to zero $\alpha_J = \alpha^{(\mathrm{blebbistatin})} = 0 < \alpha^{(\mathrm{control})}$ and $\chi_J = \chi^{(\mathrm{blebbistatin})} = 0 < \chi^{(\mathrm{control})}$ for cells being treated with blebbistatin, see Fig. S5(a). We then let the system relax to a new equilibrium state. Subsequently, to model the effect of blebbistatin wash-out, we recover the activity level of these cells being treated with blebbistatin. We provide the parameter values in simulations in Table II.

Result With our set of parameter values, the cell area and cell anisotropy are both increased in the blebbistatin-treated cells; the cell area increase is chosen to match the values observed in experiments (Fig. SX). In the blebbistatin wash-out experiment, the recovery of the actin star network leads to a progressive return of the cell area to the pre-blebbistatin treatment value (Fig. 5D). This experiment is important in setting the values of α and χ associated to the onset of the actin star network.

3. Simulation 3: cell differentiation from crypt cells

Method Here, to mimic the process of cell differentiation, the activities of all cells are set to be the same before differentiation, $\alpha_J = \alpha^{(\text{undifferentiated})}$ and $\chi_J = \chi^{(\text{undifferentiated})}$ for $J = 1, 2, 3, \cdots, N$.

We keep constant the $\alpha_J, \chi_j)$ parameters within a group of cells with a number $N_{\text{differentiated}} = 50$ at the center region of the simulation box - to mimic the onset of crypt-like cells domains - while switching the $\alpha_J, \chi_j)$ parameters to $\alpha_J = \alpha^{(\text{differentiated})}$ and $\chi_J = \chi^{(\text{differentiated})}$ within the rest of the tissue, mimicking differentiation into villus-like cells, see Fig. S6(a).

We then let the system relax to a new equilibrium state. We provide the parameter values in simulations in Table III and IV.

Result We test two possible cell differentiation paths in the (α, χ) space, see Fig. S6(b,c).

- in the cell differentiation path I differentiation path, the cells within the interior domain increase their area, akin to cells subjected to the blebbistanin treatment experiments.
- in the cell differentiation path II, the cells within the interior domain display a lower area than differentiated ones, as crypt-like cells. We also observe a progressive increase of the triangular order within the differentiated cells, see Fig. S6(g). As in experiments, the hexatic order, Eq. (**??**), remained relatively unchanged throughout the cell differentiation process, while the triangular order, Eq. (**??**), evolved significantly, see Fig. S6(f-g).

II. MODEL 2: ACS FORMATION MODELLED THROUGH ACTIN CABLE RESTORING FORCES

So far, we have considered a generic model in which the active pulling stress α_J and active tension χ_J are two independent parameters.

Here, we propose to focus on a more specific microscopic model which encompasses the observation that the actin star seemingly connects each of the junction mid-points to the cell center, see Fig. S3. We express the relation of this new model to the former one described above in terms of a linear relation between the actin star tension ξ (new model) with the active pressure α_J and active tension χ_J (former model).

New model description Here, we propose to model the actin star network through a set of active forces, denoted $\boldsymbol{T}_i$, each applied to the junction mid-points and pointing toward the cell center, $\boldsymbol{r}_C = \sum_{i\in cell} \boldsymbol{r}_i/n$, with n the number of edges of the cell. Based on the Batchelor formula [8–11], the coarse-grained active stress reads

$$\boldsymbol{\sigma}^{(\text{active})} = -\frac{1}{A}\sum_{i\in cell} \boldsymbol{s}_i \otimes \boldsymbol{T}_i. \tag{S21}$$

where $\boldsymbol{s}_i = \boldsymbol{\rho}_i + \boldsymbol{l}_i/2 = \boldsymbol{r}_i - \boldsymbol{r}_C + (\boldsymbol{r}_{i+1} - \boldsymbol{r}_i)/2 = (\boldsymbol{r}_i + \boldsymbol{r}_{i+1})/2 - \boldsymbol{r}_C$ is the length vector $\boldsymbol{s}_i$ of the i-th actin cable, assumed to connect the cell center to the junction mid-point.

Here, we focus on the case of a linear relationship between the active force $\boldsymbol{T}_i$ and the i-th actin cable vector $\boldsymbol{s}_i$

$$\boldsymbol{T}_i = -\zeta \boldsymbol{s}_i, \tag{S22}$$

where $\zeta > 0$ quantifies the contractility of the actin star network. Substituting Eq. (S22) into Eq. (S21), the active stress then takes the expression:

$$\boldsymbol{\sigma}^{(\text{active})} = \zeta \boldsymbol{W}, \tag{S23}$$

where W is what we call the mid-point cell shape tensor (Fig. S3), defined as:

$$\boldsymbol{W} = \frac{1}{A}\sum_{i\in\text{cell}} \boldsymbol{s}_i \otimes \boldsymbol{s}_i. \tag{S24}$$

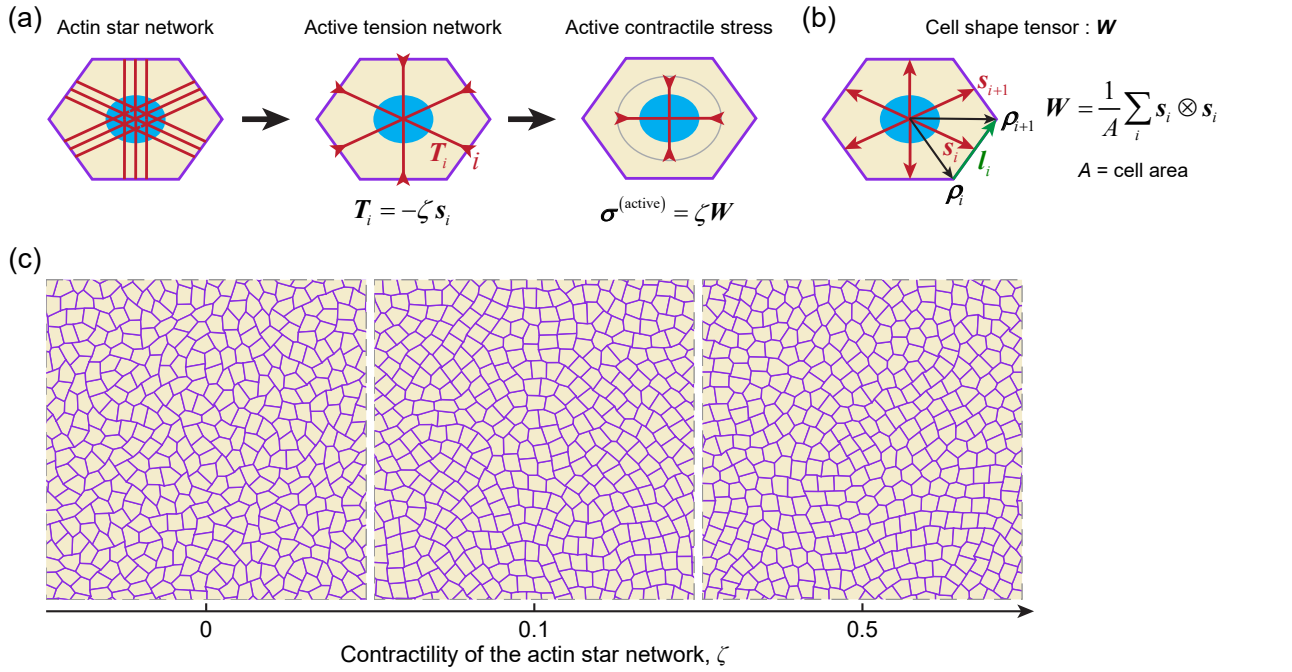

Figure S3: Alternative active stress description of the actin star network. (a, b) Model sketches of the actin star network, active stresses, and cell shape tensor. (a) Mechanical description of the actin star network contractility within a cell by active stresses, $\boldsymbol{\sigma}^{(\text{active})} = \zeta \boldsymbol{W}$ with $\zeta > 0$ quantifying the contractility level and $\boldsymbol{W}$ a cell shape tensor. (b) Sketch of the cell shape tensor $\boldsymbol{W}$. (c) Numerical simulations using the alternative stress description (Eq. (S23)). An increase in the contractility parameter ζ leads to more rounded cell shapes. Parameters: $K_A = 1$, $A_0 = 1$, $K_P = 0.02$, and $P_0 = 4$.

In particular, for a regular hexagonal cell shape, $\boldsymbol{W} = (\sqrt{3}/2)\boldsymbol{I}$.

Let us here consider a regular hexagonal cell undergoing affine transformation, $(x, y) \to (\lambda_1 x, \lambda_2 y)$, with λ_1 and λ_2 stretches along the x-axis and the y-axis. In this case, the mid-point cell shape tensor $\boldsymbol{W}$ reads

$$\boldsymbol{W} = \frac{\sqrt{3}}{2}\frac{\lambda_1}{\lambda_2}\hat{\boldsymbol{x}} \otimes \hat{\boldsymbol{x}} + \frac{\sqrt{3}}{2}\frac{\lambda_2}{\lambda_1}\hat{\boldsymbol{y}} \otimes \hat{\boldsymbol{y}}, \tag{S25}$$

while the $\boldsymbol{Q}$ tensor defined in Eq. (S10) reads:

$$\boldsymbol{Q} = \left(\frac{\lambda_1}{\sqrt{\lambda_1^2 + 3\lambda_2^2}} - \frac{1}{2}\right)\hat{\boldsymbol{x}} \otimes \hat{\boldsymbol{x}} - \left(\frac{\lambda_1}{\sqrt{\lambda_1^2 + 3\lambda_2^2}} - \frac{1}{2}\right)\hat{\boldsymbol{y}} \otimes \hat{\boldsymbol{y}}. \tag{S26}$$

For small pure shear deformations, $\lambda_1 = 1 + \varepsilon$ and $\lambda_2 = 1 - \varepsilon$ with $\varepsilon \ll 1$, we find that

$$\boldsymbol{W} \approx \frac{\sqrt{3}}{2}\boldsymbol{I} + \sqrt{3}\varepsilon(\hat{\boldsymbol{x}} \otimes \hat{\boldsymbol{x}} - \hat{\boldsymbol{y}} \otimes \hat{\boldsymbol{y}}), \tag{S27}$$

while

$$\boldsymbol{Q} \approx \frac{3}{4}\varepsilon(\hat{\boldsymbol{x}} \otimes \hat{\boldsymbol{x}} - \hat{\boldsymbol{y}} \otimes \hat{\boldsymbol{y}}). \tag{S28}$$

Thus, we find that, at first order in the pure shear amplitude,

$$\boldsymbol{\sigma}^{(\text{active})} \approx \frac{\sqrt{3}\zeta}{2}\boldsymbol{I} + \frac{4\sqrt{3}\zeta}{3}\boldsymbol{Q}. \tag{S29}$$

Comparing it to Eq. (S11) and taking $A_J = A_0$ and $P_J = P_0$, we get relationships between the contractility activity parameter ζ, α_J and χ_J:

$$\begin{cases} \alpha_J \approx -\dfrac{\sqrt{3}}{6}\zeta \\ \chi_J \approx \dfrac{8\sqrt{3}}{3}\dfrac{A_0}{P_0}\zeta \end{cases} \tag{S30}$$

We, therefore, expect that the forces defined in Eq. (S22) can be recast into the formalism of Eq. (S11): an increase in the contractility parameter ζ then maps into a decrease in α and an increase in χ; a sufficiently large increase in ζ thus can trigger a transition from a liquid to a solid regime, see Fig. S2(a) and Fig. S3(c).

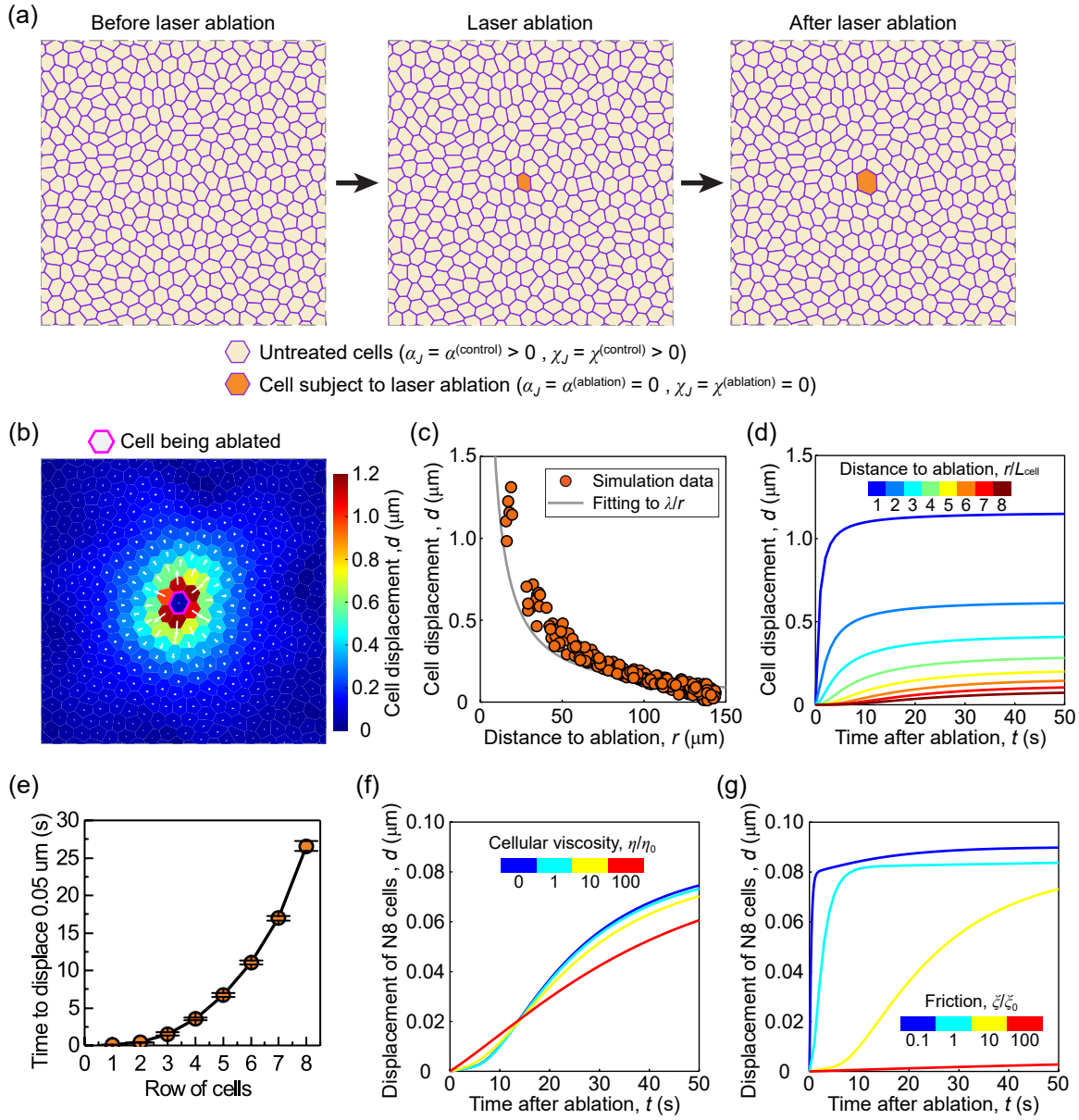

Figure S4: **Simulation 1: the laser ablation of an actin star node.** (a) Sketch of the active vertex model to simulate the laser ablation response of an intestinal epithelial monolayer. Vertex model description of an intestinal epithelial cell monolayer by a two-dimensional tiling of polygons. To mimic the effect of laser ablation, we set the activity of the cell being ablated to zero (i.e., $\alpha_J = 0$ and $\chi_J = 0$). (b-f) Simulation results of the laser ablation response of an intestinal epithelial monolayer. (b) The displacement of cells at time $t = 50$ s in response to the laser ablation (applied at $t = 0$). The color code represents the magnitude of cell displacement, while the white arrows refer to the cell displacement vector. The cell being ablated is marked by the magenta contour. (c) Scatter plot of the cell displacement magnitude as a function of the distance of the cell center to the ablation site. Symbols: simulation data. Gray solid line: fitting to λ/r with $\lambda = 13.5\ \mu\text{m}^2$ fitted by the least squares method. (d) The average displacement magnitude of cells at the k-th row as a function of time t after ablation. The cells at the k-th row are defined by the distance d of the cell center to the ablation site if it satisfies $k - 1/2 < d/L_{\text{cell}} < k + 1/2$ with $L_{\text{cell}} = 10\ \mu\text{m}$ being the cell size. (e) Time to displace 0.05 μm, $t_{0.05\ \mu\text{m}}$, as a function of the row of cells (i.e., distance to the laser ablation site). Averaged over $n = 5$ independent simulations. Data = mean $\pm$ SD. (f) The average displacement magnitude of cells at the 8-th row (denoted N8 cells) as a function of time t after ablation, for different levels of cellular viscosities expressed in the unit of $\eta_0 = 0.01\ \text{nN} \cdot \text{s} \cdot \mu\text{m}^{-1}$, with fixed friction $\xi = 0.1\ \text{nN} \cdot \text{s} \cdot \mu\text{m}^{-1} = 10\eta_0$; (g) The average displacement magnitude of cells at the 8-th row (denoted N8 cells) as a function of time t after ablation, for different levels of friction expressed in units of $\xi_0 = 0.01\ \text{nN} \cdot \text{s} \cdot \mu\text{m}^{-1}$, with fixed cellular viscosity $\eta = 0.01\ \text{nN} \cdot \text{s} \cdot \mu\text{m}^{-1} = \xi_0$. Other parameters are set in Table I.

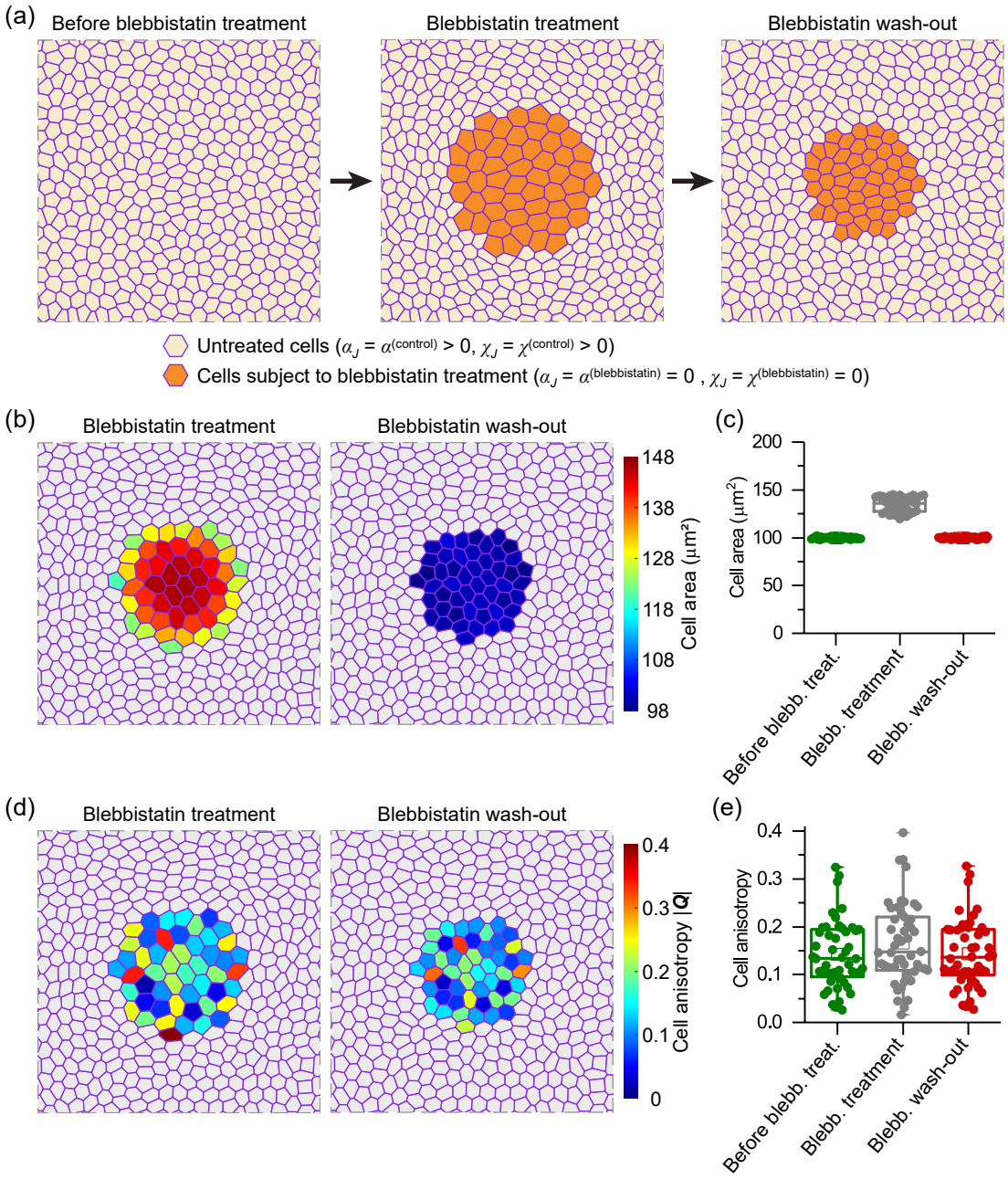

Figure S5: **Simulation 2: contractility recovery by blebbistatin wash-out.** (a) Sketch of the active vertex model to simulate the effect of blebbistatin treatment and the subsequent contractility recovery process by blebbistatin wash-out. The blebbistatin treatment is mimicked by a decrease in the contractility activity of the actin star network within the cells being treated. The blebbistatin wash-out effect is mimicked by recovering the contractility activity with the cells being treated. (b-e) Simulation results. (b) The cell area field after blebbistatin treatment (*left*) and the cell area field after blebbistatin wash-out (*right*). Here, we show the area of cells being treated. (c) Statistical analysis of cell area before blebbistatin treatment, after blebbistatin treatment, and after blebbistatin wash-out. The cell area are 99.8 ± 1.0 μm^2 (mean $\pm$ S.D.), 134.1 ± 7.7 μm^2 (mean $\pm$ S.D.) and 99.9 ± 1.0 μm^2, in turn. $n = 50$ cells. (d) The cell anisotropy field after blebbistatin treatment (*left*) and the cell area field after blebbistatin wash-out (*right*). Here, we show the anisotropy of cells being treated. (e) Statistical analysis of cell anisotropy before blebbistatin treatment, after blebbistatin treatment, and after blebbistatin wash-out. The cell anisotropy are 0.142 ± 0.070 μm^2 (mean $\pm$ S.D.), 0.165 ± 0.084 μm^2 (mean $\pm$ S.D.) and 0.143 ± 0.070 μm^2, in turn. $n = 50$ cells. Simulation parameters are provided in Table II.

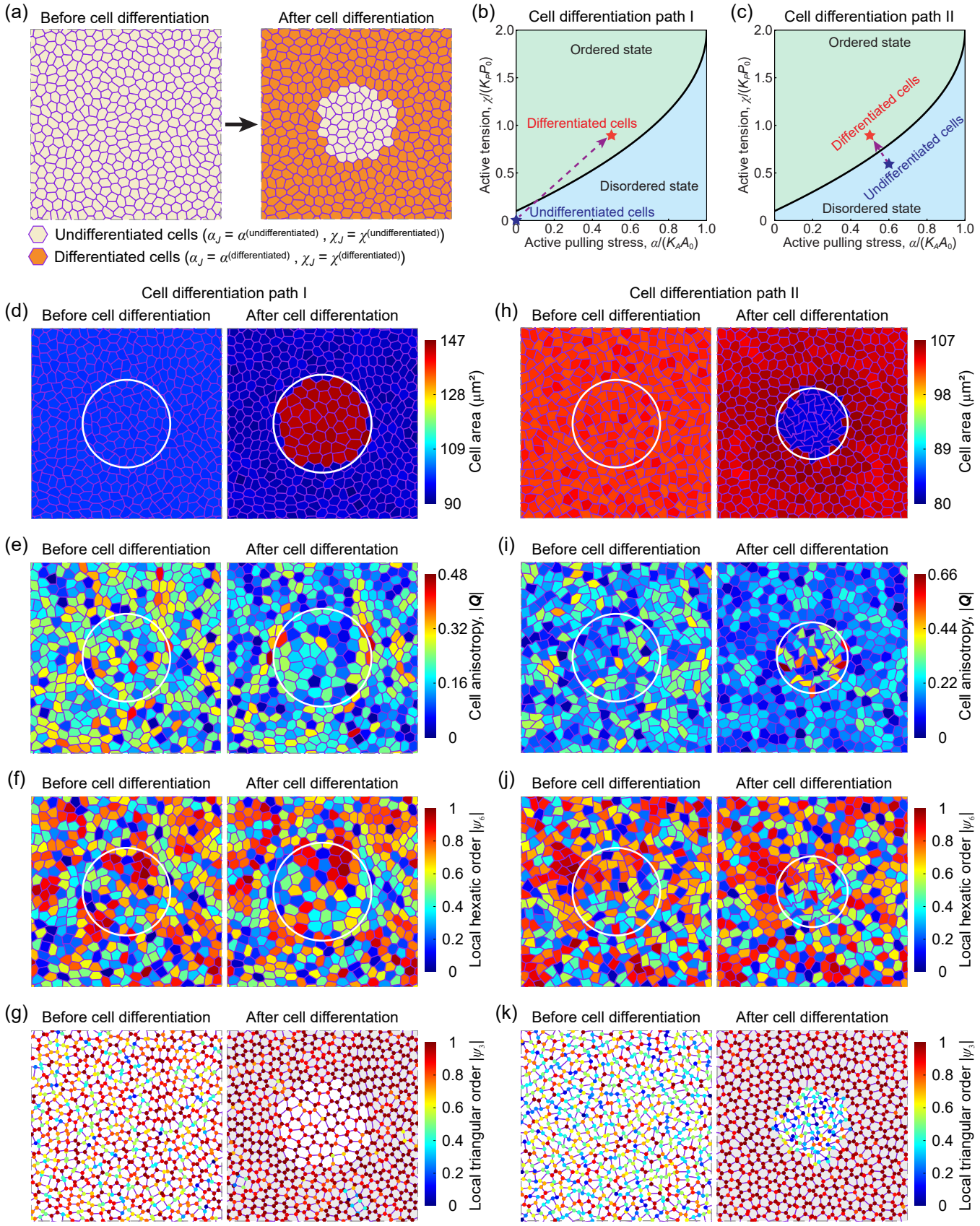

Figure S6: (Caption on the next page.)

Figure S6: (Previous page.) **Simulation 3: cell differentiation from crypt-like cells to villus-like cells.** (a) Sketch of the active vertex model to simulate the process of cell differentiation from crypt-like cells (light yellow) to villus-like cells (orange). Initially, cells are all the same. We mimic the cell differentiation effect by selecting a group of cells and setting up a different level of activity. (b, c) Two possible cell differentiation paths in the (α , χ) space. (d-k) Simulation results of (d, h) the cell area field, (e, i) the anisotropy field, (f, j) the local hexatic order parameter field, and (g, k) the local triangular order parameter field (*left*) before and (*right*) after cell differentiation. Here, the cell anisotropy is quantified by the magnitude of the anisotropic cell shape tensor $|\boldsymbol{Q}|$. In (g, k), differentiated cells are marked as grey. Results (d-g) correspond to the path shown in (b); while results (h-k) correspond to the path shown in (c). Parameter values used in such simulations are given in Table III and IV.

TABLE I: List of default parameter values used in our simulation 1 of laser cell ablation, Sec. I C 1.

Parameter	Description	Value
$\ell = \sqrt{A_0}$	Length scale	10 μm
τ	Time scale	0.1 s
$f = K_A A_0^{3/2}$	Force scale	1 nN
K_A	Cell area stiffness	10^6 N $\cdot$ m^{-3}
A_0	Preferred cell area	100 μm^2
K_P	Cell perimeter stiffness	0.002 nN $\cdot$ μm^{-1}
P_0	Preferred cell perimeter	40 μm
ξ	Cell-substrate friction	0.1 nN $\cdot$ s $\cdot$ μm^{-1}
η	Viscosity of cells	0.01 nN $\cdot$ s $\cdot$ μm^{-1}
$\alpha^{(\text{control})}$	Active pulling stress level of control cells	0.05 nN $\cdot$ μm^{-1}
$\alpha^{(\text{ablation})}$	Active pulling stress level of the ablated cell	0
$\chi^{(\text{control})}$	Active tension level of control cells	0.064 nN
$\chi^{(\text{ablation})}$	Active tension level of the ablated cell	0
Δt	Simulation time step	0.001 s

TABLE II: List of default parameter values used in simulation 2, contractility recovery, Sec. I C 2.

Parameter	Description	Value
$\ell = \sqrt{A_0}$	Length scale	10 μm
τ	Time scale	0.1 s
$f = K_A A_0^{3/2}$	Force scale	1 nN
K_A	Cell area stiffness	10^6 N $\cdot$ m^{-3}
A_0	Preferred cell area	100 μm^2
K_P	Cell perimeter stiffness	0.002 nN $\cdot$ μm^{-1}
P_0	Preferred cell perimeter	40 μm
ξ	Cell-substrate friction	0.1 nN $\cdot$ s $\cdot$ μm^{-1}
η	Viscosity of cells	0.01 nN $\cdot$ s $\cdot$ μm^{-1}
$\alpha^{(\text{blebbistatin})}$	Active pulling stress level of cells after blebbistatin treatment	0
$\alpha^{(\text{control})}$	Active pulling stress level of cells before blebbistatin treatment or after blebbistatin wash-out	0.05 nN $\cdot$ μm^{-1}
$\chi^{(\text{blebbistatin})}$	Active tension level of cells after blebbistatin treatment	0
$\chi^{(\text{control})}$	Active tension level of cells before blebbistatin treatment or after blebbistatin wash-out	0.064 nN
Δt	Simulation time step	0.001 s

TABLE III: List of default parameter values used in simulation 3, cell differentiation (path I), Sec. I C 3.

Parameter	Description	Value
$\ell = \sqrt{A_0}$	Length scale	10 μm
τ	Time scale	0.1 s
$f = K_A A_0^{3/2}$	Force scale	1 nN
K_A	Cell area stiffness	10^6 N $\cdot$ m^{-3}
A_0	Preferred cell area	100 μm^2
K_P	Cell perimeter stiffness	0.002 nN $\cdot$ μm^{-1}
P_0	Preferred cell perimeter	40 μm
ξ	Cell-substrate friction	0.1 nN $\cdot$ s $\cdot$ μm^{-1}
η	Viscosity of cells	0.01 nN $\cdot$ s $\cdot$ μm^{-1}
$\alpha^{(\text{undifferentiated})}$	Active pulling stress level of undifferentiated cells (crypt-like cells)	0
$\alpha^{(\text{differentiated})}$	Active pulling stress level of differentiated cells (villus-like cells)	0.05 nN $\cdot$ μm^{-1}
$\chi^{(\text{undifferentiated})}$	Active tension level of undifferentiated cells (crypt-like cells)	0
$\chi^{(\text{differentiated})}$	Active tension level of differentiated cells (villus-like cells)	0.064 nN
Δt	Simulation time step	0.001 s

TABLE IV: List of default parameter values used in simulation 3, cell differentiation (path II), Sec. I C 3.

Parameter	Description	Value
$\ell = \sqrt{A_0}$	Length scale	10 μm
τ	Time scale	0.1 s
$f = K_A A_0^{3/2}$	Force scale	1 nN
K_A	Cell area stiffness	10^6 N $\cdot$ m^{-3}
A_0	Preferred cell area	100 μm^2
K_P	Cell perimeter stiffness	0.002 nN $\cdot$ μm^{-1}
P_0	Preferred cell perimeter	40 μm
ξ	Cell-substrate friction	0.1 nN $\cdot$ s $\cdot$ μm^{-1}
η	Viscosity of cells	0.01 nN $\cdot$ s $\cdot$ μm^{-1}
$\alpha^{(\text{undifferentiated})}$	Active pulling stress level of undifferentiated cells (crypt-like cells)	0.06 nN $\cdot$ μm^{-1}
$\alpha^{(\text{differentiated})}$	Active pulling stress level of differentiated cells (villus-like cells)	0.05 nN $\cdot$ μm^{-1}
$\chi^{(\text{undifferentiated})}$	Active tension level of undifferentiated cells (crypt-like cells)	0.056 nN
$\chi^{(\text{differentiated})}$	Active tension level of differentiated cells (villus-like cells)	0.064 nN
Δt	Simulation time step	0.001 s

[1] T. Nagai and H. Honda, Philosophical Magazine B **81**, 699 (2001).
[2] R. Farhadifar, J. C. Röper, B. Algouy, S. Eaton, and F. Jülicher, Current Biology **17**, 2095–2104 (2007).
[3] S. Alt, P. Ganguly, and G. Salbreux, Philosophical Transactions of the Royal Society B: Biological Sciences **372**, 20150520 (2017).
[4] C. Fu, F. Dilasser, S.-Z. Lin, M. Karnat, A. Arora, H. Rajendiran, H. T. Ong, N. M. H. Brenda, S. W. Phow, T. Hirashima, M. Sheetz, J.-F. Rupprecht, S. Tlili, and V. Viasnoff, bioRxiv , 2023.12.04.570034 (2024).
[5] A. G. Fletcher, M. Osterfield, R. E. Baker, and S. Y. Shvartsman, Biophysical Journal **106**, 2291–2304 (2014).
[6] D. Bi, J. Lopez, J. Schwarz, and M. L. Manning, Nature Physics **11**, 1074–1079 (2015).
[7] S.-Z. Lin, S. Ye, G.-K. Xu, B. Li, and X.-Q. Feng, Biophysical Journal **115**, 1826 (2018).
[8] S.-Z. Lin, M. Merkel, and J.-F. Rupprecht, Physical Review Letters **130**, 058202 (2023).
[9] G. Batchelor, Journal of Fluid Mechanics **41**, 545 (1970).
[10] A. W. C. Lau and T. C. Lubensky, Physical Review E **80**, 011917 (2009).
[11] S.-Z. Lin, M. Merkel, and J.-F. Rupprecht, The European Physical Journal E **45**, 4 (2022).
[12] S. Sonam, L. Balasubramaniam, S.-Z. Lin, Y. M. Y. Ivan, I. Pi-Jaumà, C. Jebane, M. Karnat, Y. Toyama, P. Marcq, J. Prost, *et al.*, Nature Physics **19**, 132 (2023).
[13] A. Nestor-Bergmann, G. Goddard, S. Woolner, and O. E. Jensen, Mathematical Medicine and Biology: A Journal of the IMA **35**, i1 (2018).
[14] K. Bambardekar, R. Clément, O. Blanc, C. Chardès, and P.-F. Lenne, Proceedings of the National Academy of Sciences of the United States of America **112**, 1416 (2015).